Optical and mid-infrared neon abundance determinations in star-forming regions

Oli L. Dors Jr,[1]* Guillermo F. Hägele,[2,3] Mónica V. Cardaci,[2,3]
Enrique Pérez-Montero,[4] Ângela C. Krabbe,[1] José M. Vílchez,[4]
Dinalva A. Sales,[5] Rogério Riffel[5] and Rogemar A. Riffel[6]

[1]*Universidade do Vale do Paraíba, Av. Shishima Hifumi, 2911, Cep 12244-000, São José dos Campos, SP, Brazil*
[2]*Consejo Nacional de Investigaciones Científicas y Técnicas (CONICET), Argentina*
[3]*Facultad de Ciencias Astronómicas y Geofísicas, Universidad Nacional de La Plata, Paseo del Bosque s/n, 1900 La Plata, Argentina*
[4]*Instituto de Astrofísica de Andalucía (CSIC), PO Box 3004, E-18080 Granada, Spain*
[5]*Universidade Federal do Rio Grande do Sul, IF, CP 15051, Porto Alegre 91501-970, RS, Brazil*
[6]*Universidade Federal de Santa Maria, Av. Roraima 1000, Cep 97105-900, Santa Maria, Brazil*

ABSTRACT
We have used observational spectroscopic data of star-forming regions compiled from the literature and photoionization models to analyse the neon ionic abundances obtained using both optical and mid-infrared emission lines. Comparing Ne^{++}/H^+ ionic abundances from distinct methods, we have found that, on average, the abundances obtained via infrared emission lines are higher than those obtained via optical lines, by a factor of 4. Photoionization models with abundance variations along the radius of the hypothetical nebula provide a possible explanation for a large part of the difference between ionic abundances via optical and infrared emission lines. The ionization correction factor (ICF) for the neon is obtained from direct determinations of ionic fractions using infrared emission lines. We derive a constant Ne/O ratio ($\log Ne/O \approx -0.70$) for a large range of metallicities, independently of the ICF used to compute the neon total abundance.

Key words: galaxies: abundances – galaxies: evolution – galaxies: formation – galaxies: general – galaxies: ISM.

1 INTRODUCTION

The gas phase metallicity determinations in star-forming regions have been used to study the cosmic evolution of galaxies as well as to provide observational constraints on model parameters of galaxy formation.

In particular, oxygen is the element most widely used for this purpose, because prominent emission lines from their main ionic stages are present in the optical spectra of star-forming regions (e.g. Kennicutt, Bresolin & Garnett 2003; Krabbe & Copetti 2006; Hägele et al. 2008). For the remaining elements with bright emission lines (e.g. N, S, Ne and Ar), not all their ionic stages are observed in the optical spectrum. Thus, their total abundances can only be calculated by using ionization correction factors (ICFs), as proposed by Peimbert & Costero (1969).

Among the α-elements, Ne is found to be of great importance because it is one of the noble gases and it does not combine with itself or with other chemical species in the formation of molecules, and thus dust grains. This makes the abundance determination of

this element quite suitable for the study of the chemical evolution of star-forming regions, because it does not depend on depletion factors on to dust grains. It is accepted that Ne and O are mainly produced in stars more massive than 10 $M_\odot$ (see Woosley & Weaver 1995). Therefore, it is expected that the abundances of Ne and O should closely trace one another (Crockett et al. 2006), and a constant Ne/O abundance ratio over a wide range of O/H abundance should be found. However, the recent deep spectroscopy of a large sample of low-metallicity emission-line galaxies (ELGs) by Guseva et al. (2011) has revealed a slight increase of Ne/O with O/H. Similar results have also been found by Wang & Liu (2008), using the O and Ne abundances of a sample of planetary nebulae and H II regions. In contrast, Pérez-Montero et al. (2007) have derived a new ICF for Ne, using a photoionization model grid. For the high-metallicity regime, they have found a slight decrease in Ne/O with O/H for a large sample of star-forming regions.

In any case, the derivation of the total Ne abundance has been shown to be uncertain because of the difficulties in estimating its ICF. The estimation of the total Ne abundance in the optical is performed via the observation of the [Ne III]λ3869 Å emission line, which is mainly present in star-forming regions with a high-ionization degree. Usually, an ICF(Ne^{++}) is assumed that is a

* E-mail: olidors@univap.br

function of the O/O^{++} ratio, also derived from optical emission lines. However, the optical [Ne III] line is rarely observed in metal-rich objects (see Bresolin et al. 2005), where most of the Ne is in the form of Ne^{+}, so the ICFs are not well constrained in this regime (Kennicutt et al. 2003). This problem can be alleviated by the use of infrared (IR) fine-structure lines (Vermeij & van der Hulst 2002). In this context, both the *Infrared Space Observatory* (*ISO*; Kessler et al. 1996) and the *Spitzer Space Telescope* have allowed the observation of bright mid-IR emission lines in star-forming regions, such as [Ne II]12.81 μm and [Ne III]15.56 μm, and the determination of the total Ne abundance simply by summing the corresponding ionic fractions. For instance, Vermeij & van der Hulst (2002) have used the optical and mid-IR data of H II regions located in the Magellanic Clouds (see also Vermeij et al. 2002) to determine the O, S and Ne abundances in these objects. They found large discrepancies between the Ne^{++} abundances obtained via IR lines with those obtained using optical temperature determinations. They have pointed out that the classical approximation, ICF(Ne^{++}) = O/O^{++} (Peimbert & Costero 1969), seems to underestimate the true Ne abundance (see also Pérez-Montero et al. 2007). However, because of the large scatter and uncertainty in the Ne^{++} ionic fraction of their data, no conclusion could be drawn about the reliability of the optical ICF for Ne. The same results were obtained by Kennicutt et al. (2003), who combined the ionic abundances derived by Vermeij & van der Hulst (2002) and Willner & Nelson-Patel (2002) for H II regions located in M33. However, they were not able to derive a functional form for the ICF(Ne^{++}), because of the large scatter of the available data and the very few measurements for low-ionization regions. Fortunately, a large number of mid-IR and optical data of star-forming regions are currently available in the literature. This enables us to make a direct determination of the optical ICF for Ne and a comparison among abundances obtained from distinct methods, yielding a more reliable conclusion about the total Ne abundance.

Our main goal in this paper is to examine the Ne abundance of star-forming regions, investigating the abundance discrepancy found by using different methods and obtaining a reliable ICF in the optical for this element. To do this, we have compiled observed optical and IR emission-line fluxes from the literature to derive the Ne ionic abundances. A photoionization model grid was also used in this analysis. The paper is organized as follows. In Section 2, we describe the observational data used in the paper, and we perform an analysis of the selected sample. We give a description of the photoionization models in Section 3. We present the procedures to determine the ionic abundances in Section 4. We compare the neon ionic abundances obtained from distinct methods in Section 5. In Section 6, we present the ICFs computed for Ne^{++} and applied to the data set. We give our conclusions of the outcomes in Section 7.

2 OBSERVATIONAL DATA

2.1 Sample description

The optical and IR emission-line fluxes of a sample of ELGs – including H II galaxies, Wolf–Rayet galaxies, blue compact galaxies (BCGs) and dwarf galaxies (DGs) – and H II regions were compiled from the literature. Their emission-line intensities were already reddening corrected in the studies from which we have taken the data. For most of the data, this was done by using the ratio Hα/Hβ. In some cases, where Hα was not present in the spectra, the reddening coefficient was obtained from another hydrogen line (e.g. the data of Crockett et al. 2006).

The selection criterion was the presence of flux measurements of the optical [O II]λ3727, [Ne III]λ3869, Hβ and [O III]λ5007 emission lines. We have also compiled the line intensities of [O III]λ4363, Hα, [N II](λ5755,λ6548,λ6584) and [S III](λ6717,λ6731) when they were available. Regarding mid-IR emission lines, we selected 50 ELGs and 93 H II regions located in the Magellanic Clouds, M101, M33 and M83. whose [Ne II]12.81 μm and [Ne III]15.56 μm emission lines had been measured. The optical data were obtained by the use of long-slit, echelle and multi-object spectroscopy (MOS), while the IR data were obtained with the *ISO* and *Spitzer*.

In the optical, we used the [O III]λ5007/Hβ versus [N II]λ6584/Hα and [O III]λ5007/Hβ versus [S II](λ6716+λ6731)/Hα diagnostic diagrams (Fig. 1) to distinguish objects ionized by massive stars from those containing an active galactic nucleus (AGN) and/or gas excited by shocks. To separate the distinct classes of objects, we used the criteria proposed by Kewley et al. (2006), where all objects with log [O III]λ5007/Hβ < 0.61/[log[N II]λ6584/Hα −0.05] + 1.3 and log[O III]λ5007/Hβ < 0.72/[log[S II]λ(6717+λ6731)/Hα − 0.32] + 1.3 have massive stars as their main ionization mechanism. From this analysis, we discarded 15 objects, yielding a sample with 522 ELGs and 212 H II regions.

Because of the non-homogeneity of the compiled data, according to the available emission lines measured for each object, we divided the sample into five groups, as follows.

Group A: optical emission lines, including those needed to directly estimate the electron temperatures and abundances.
Group B: [O II]λ3727, [Ne III]λ3869, Hβ, [O III]λ5007 (the optical selection criterion) and [O III]λ4363.
Group C: optical emission lines, except for those sensitive to the temperature, that is, [O III]λ4363, [O II]λ7325 and [N II]λ5755.
Group D: only the [O II]λ3727, [Ne III]λ3869, Hβ and [O III]λ5007 emission lines (just fulfilling the optical selection criterion).
Group E: the IR emission lines.

Table 1 lists the bibliographic references of the sample, the number of objects taken from each work, their nature, the observational technique used during the data acquisition and the group(s) to which the data belong. The objects in the A, B and E groups allow the computation of the ionic abundances and the ICFs from several methods used in this paper, while the ones in the C and D groups only enable a more accurate comparison between the data and the photoionization models to obtain a theoretical neon ICF.

To investigate the discrepancy between the neon ionic abundances from optical and IR emission lines, we selected the objects in our sample for which we can obtain a direct estimation of, at least, an electron temperature. These belonging to the optical groups A and B, and also to the IR group E. The subsample contains 23 objects, as listed in Table 2, together with the corresponding optical and IR references. It is worth emphasizing that for the objects in this subsample only, we can estimate the oxygen and neon ionic abundances via optical lines and the neon ones via IR lines.

For the H II regions located in the Magellanic Clouds, we have converted the Brβ fluxes, directly measured from the observations by Vermeij & van der Hulst (2002), into Hβ fluxes, using the emissivities of Storey & Hummer (1995). We did not use the Huα emission line at 10.52 μm, even though it is the closest hydrogen line to the mid-IR Ne lines, because for our compiled sample it is generally blended with an H$_2$ emission line. For the remaining sources, we considered the observed Hβ fluxes. A similar procedure was carried out by Wu et al. (2008) in their study of elemental abundances of BCGs using *Spitzer* observations.
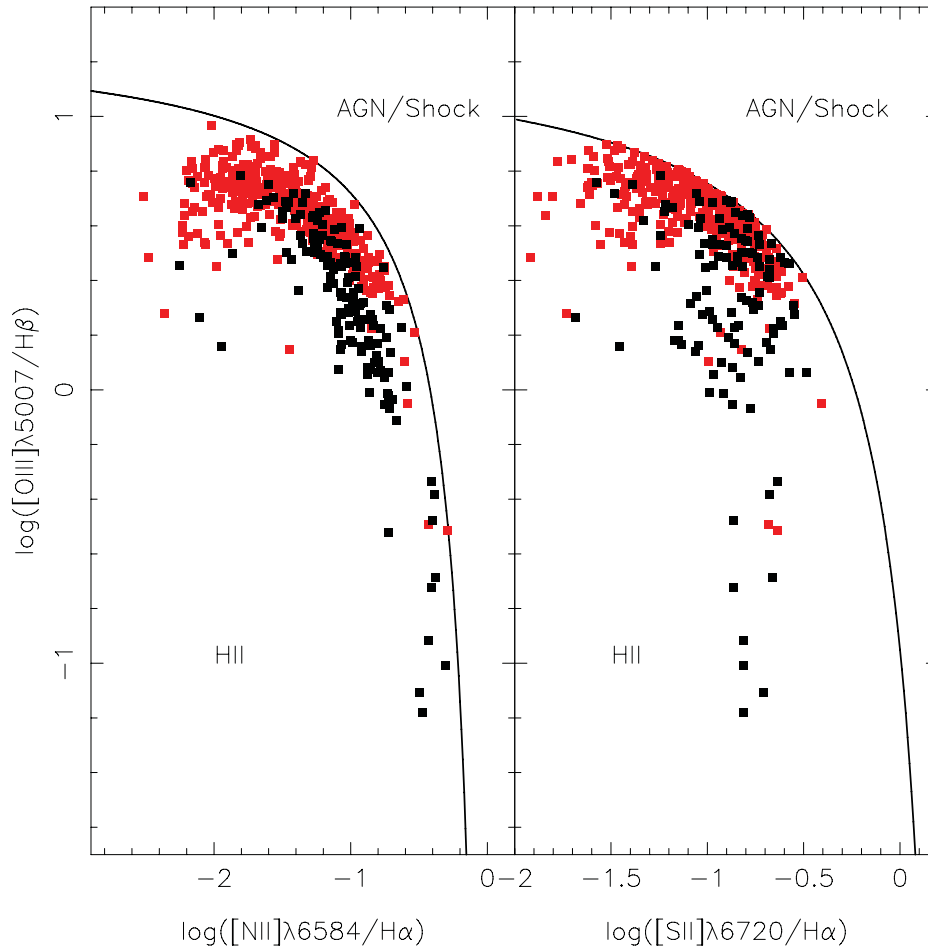
Figure 1. Diagnostic diagrams for [O III]λ5007/Hβ versus [N II]λ6584/Hα (left) and [O III]λ5007/Hβ versus [S II](λ6716+λ6731)/Hα (right). The solid lines, taken from Kewley et al. (2006), separate objects ionized by massive stars from those containing active nuclei and/or shock-excited gas, as indicated. The black squares represent H II regions and the red squares denote the ELGs compiled from the literature.

2.2 Analysis of the sample

Over the years, several authors have compiled the spectroscopy data of star-forming regions from the literature in order to derive correlations between the macroscopic properties of these objects (e.g. Pilyugin, Vílchez & Contini 2004), or they have suggested oxygen abundance calibrations using strong emission lines (e.g. Nagao, Maiolino & Marconi 2006; Pérez-Montero & Contini 2009). However, the use of data sets obtained with different instrumentation and observational techniques, and including different objects, such as whole galaxies, galaxy nuclei and individual H II regions (i.e. non-homogeneous data), could lead to biased results. In what follows, we investigate the possible sources of biases introduced in the present study because of the heterogeneity of our data set.

2.2.1 Aperture effects

Differences between the measurement apertures used in the optical and IR observations could contribute significantly to the discrepancies found between the optical and IR abundance determinations (Vermeij & van der Hulst 2002). This is because many physical properties (e.g. stellar populations, metallicity, extinction) of galaxies vary with the galactocentric radius (Moustakas & Kennicutt 2006a) or along nebulae (Oey et al. 2000). Kewley, Jansen & Geller (2005) have presented a detailed analysis of the effect of aperture

size on the star formation rate, metallicity and reddening determinations for galaxies selected from the Nearby Field Galaxy Survey. They have found that systematic and random errors from aperture effects can arise if fibres capture less than 20 per cent of the galaxy light. Most of the star-forming regions in our sample can be treated as point sources, and almost all the object extensions are observed. Therefore, this effect is negligible for these objects. For the spatially resolved Magellanic H II regions in our sample (see Table 2), this effect could play a more important role, as already pointed out by Vermeij & van der Hulst (2002). However, because our aim is to study the discrepancy found for the Ne^{++} ionic abundances, and because this ion is not expected to be formed in the extended low-surface brightness zones around star-forming regions, aperture effects are not an important factor.

2.2.2 Reddening correction

There are several ways to determine the reddening correction to be applied to the observed emission-line fluxes, depending on the available information and the ad hoc assumptions (e.g. the use of different ratios involving hydrogen emission-line fluxes, the use of different extinction curves and the use of a wide spectral range). All these facts could introduce some bias in our results. To investigate this effect, in Fig. 2 we plot the Hα/Hβ ratios against the ionization

Table 1. Bibliographic references for the compiled sample.

ID	Reference	Object type	Number	Technique	Group
1	Lee, Salzer & Melbourne (2004)	KISS galaxy	13	Long-slit	A
2	Vílchez & Iglesias-Páramo (2003)	DG	4	Long-slit	A
3	Hägele et al. (2006)	H II galaxy	3	Long-slit	A
4	Hägele et al. (2008)	H II galaxy	6	Long-slit	A
5	Hägele et al. (2011)	H II galaxy	2	Long-slit	A
6	Skillman, Terlevich & Melnick (1989)	DG	2	Long-slit	A
7	Thuan & Izotov (2005)	BCG	26	Long-slit	B
8	Masegosa, Moles & Campos-Aguilar (1994)	H II galaxy	99	Long-slit	A
9	Papaderos et al. (2008)	H II galaxy	24	Long-slit	A
10	Kobulnicky, Kennicutt & Pizagno (1999)	H II galaxy	7	Long-slit	A
11	Izotov, Chaffee & Green (2001)	BCG	2	Long-slit	A
12	Izotov & Thuan (2004)[a]	BCG	33	Long-slit	A
13	Izotov & Thuan (1998)[a]	BCG	17	Long-slit	A
14	Izotov et al. (2006b)[a]	H II galaxy	1	Long-slit	A
15	Izotov, Thuan & Lipovetsky (1997)[a]	BCG	28	Long-slit	A
16	Izotov, Thuan & Lipovetsky (1994)[a]	BCG	10	Long-slit	A
17	Izotov et al. (2006a)	BCG	125	Long-slit	A
18	Bergvall & Östlin (2002)[a]	BCG	3	Long-slit	A
19	Guseva, Izotov & Thuan (2000)[a]	W–R galaxy	8	Long-slit	A
20	Guseva et al. (2011)	H II galaxy	59	Long-slit	A
21	Guseva et al. (2007)[a]	H II galaxy	33	Long-slit	B
22	López-Sánchez & Esteban (2009)	W–R galaxy	17	Long-slit	A
23	Kobulnicky et al. (1997)	H IIR	3	Long-slit	A
24	Garnett et al. (1997)	H II region	7	Long-slit	A
25	Kennicutt et al. (2003)	H II region	20	Long-slit/echelle	A
26	van Zee et al. (1998)	H II region	58	Long-slit	C
27	Vílchez et al. (1988)	H II region	4	Long-slit	A, C
28	Kwitter & Aller (1981)	H II region	6	Slit	A, C
29	Bresolin et al. (2009)	H II region	28	MOS	A, C
30	Lee & Skillman (2004)	H II region	15	Long-slit	A, C
31	Bresolin, Garnett & Kennicutt (2004)	H II region	8	MOS	C
32	McCall, Rybski & Shields (1985)	H II region	20	Long-slit	A, C, D
33	van Zee (2000)	H II region	2	Long-slit	A
34	Bresolin (2011)	H II region	19	MOS	D
35	Esteban et al. (2009)	H II region	9	Long-slit	A, C
36	Crockett et al. (2006)	H II region	10	Long-slit	B, D
37	Torres-Peimbert, Peimbert & Fierro (1989)[a]	H II region	3	Long-slit	A, C
38	Engelbracht et al. (2008)	H II galaxy	41	*Spitzer*	E
39	Wu et al. (2008)	BCG	9	*Spitzer*	E
40	Gordon et al. (2008)	H II region	7	*Spitzer*	E
41	Vermeij et al. (2002)[a]	H II region	7	*ISO*	A, C, E
42	Lebouteiller et al. (2008)	H II region	31	*Spitzer*	E
43	Rubin et al. (2008)	H II region	24	*Spitzer*	E
44	Rubin et al. (2007)	H II region	24	*Spitzer*	E

[a]These are the papers from which the Hβ fluxes were obtained in order to compute the neon ionic abundances.

degree parametrized by the [O III]λ5007/[O III]λ3727 ratio (e.g. Dors & Copetti 2003; Morisset et al. 2004) for the objects belonging to our sample. In this figure, we can see very few points ($\sim$3 per cent of ELGs and $\sim$6 per cent of H II regions) out of the range of the expected values of the Hα/Hβ ratio, considering the theoretical values of Storey & Hummer (1995) for temperatures between 5000 and 20 000 K, which are typical values for star-forming regions. Thus, we can conclude that the differences in the reddening correction do not affect any statistical result obtained in this work.

2.2.3 Instrumentation and observational techniques

The data compiled from the literature were acquired using different instrumentation and observational techniques. This could yield an additional scatter in the abundance determinations computed in this work, which might lead to biased results. For example, if emission lines with a broad component are present in low-resolution spectra these will not be detected, and several physical properties obtained from these lines will be unreliable, such as abundance determinations (see Hägele et al. 2013, and references therein). Also, the heavy element abundance determinations from spectra with low signal-to-noise ratios can be overestimated (Wesson, Stock & Scicluna 2012). However, discrepancies in emission-line ratios estimated for a given object observed using different techniques, ranging from about 0.03 to 0.1 dex (Dors & Copetti 2005), translate into a few per cent in the uncertainties of ionic abundance determinations. For example, if this discrepancy in the line ratio [O III](λ5007+λ4959)/λ4363 is 0.06 dex, the electron temperature derived using the different observations differs by about 400 K, yielding a log(Ne/O) variation of about 0.1 dex. This value is of the order of the intrinsic scatter found for uniform samples studied using data obtained with the

Table 2. Objects with neon abundances determined via optical and IR emission-line intensities.

Object	Reference[a]	
	Optical	IR
ELGs		
I Zw 18	15	38
Haro 11	18	38
UM 420	13	38
Mrk 1450	16	38
NGC 4861	15	38
UM 448	13	38
Mrk 930	13	38
Mrk 162	13	38
NGC 1140	12	38
UM 461	13	39
UM 462	13	38
Tol2138-405	21	38
IIZw 40	19	38
SBS 0335–052E	14	38
M101 H II regions		
NGC 5455	37	40
NGC 5461	37	40
NGC 5471	37	40
Magellanic H II regions		
N160A1	41	41
N160A2	41	41
N157B	41	41
N4A	41	41
N66	41	41
N81	41	41

[a]The reference number is according to the ID listed in Table 1.

same instrumentation (see Kennicutt et al. 2003). When no systematic effects in the calibrations and data reduction exist, the physical properties derived using data obtained with different observational techniques should be the same. For example, the physical parameters estimated for the star-forming knots of Haro 15 are in very good agreement when derived using long-slit and echelle data (López-Sánchez & Esteban 2009; Hägele et al. 2012).

2.2.4 Nature of the sources

Our sample is composed of objects with different morphology and sizes, and yet they all have young and massive stellar clusters as their main ionization sources. The shape of the emission-line spectra of the objects in our sample is dominated by the ionizing fluxes from these massive stars. Therefore, the same measurement and analysis techniques can be applied to derive the temperatures, densities and chemical composition of their interstellar gas (Hägele et al. 2006).

In general, the H II regions and ELGs are located in the same zone in diagnostic diagrams (e.g. Baldwin, Phillips & Terlevich 1981), implying that similar ionization mechanisms are taking place in these two different types of object (see Fig. 1). Other ionizing mechanisms could be present, according to the evolutionary stages and the nature of the objects, such as galactic winds resulting from supernovae (e.g. Tang et al. 2009), the contribution to the hydrogen emission fluxes by diffuse ionized gas (e.g. Calzetti et al. 2004; Moustakas & Kennicutt 2006b; Oey et al. 2007) and/or the presence of obscured AGNs (Kewley et al. 2001), or even the effects of the presence of multiple kinematical components in the emission-line

profiles (e.g. Firpo et al. 2010, 2011; Hägele et al. 2010; Amorín et al. 2012, and references therein). The statistical contribution of these mechanisms is similar for the different types of object, and they do not yield any bias on the physical conditions of the objects obtained in the present work.

3 PHOTOIONIZATION MODELS

To estimate the ICF for Ne using photoionization models, we compared the results of a grid of models performed using the CLOUDY/8.0 code (Ferland et al. 1998) with the observational data sample. We used data from the groups A, B, C, D and E, which include all objects with optical and IR emission lines available (i.e. 734 objects). For the comparison, we used the diagnostic diagrams [O III]λ5007/[O II]λ3727 versus [N II]λ6584/[O II]λ3727, [Ne III]λ3869/Hβ versus [O II]λ3727/Hβ, [N II]λ6584/Hα versus [S II]λ6720/Hα and [Ne III]15.56 μm/[Ne II]12.81 μm versus [O III]λ5007/[O II]λ3727 (see Fig. 3). The ICF values were obtained from the model results, which better reproduce the observational data.

The model grid was built following the same procedures as Dors et al. (2011), with metallicities of Z = 2.0, 1.0, 0.6, 0.4, 0.02 and 0.01 Z$_\odot$, and the logarithm of the ionization parameter U from -3.5 to -1.5 dex, with a step of -0.5 dex. For each model, the ionizing source was assumed to be a stellar cluster with a spectral energy distribution obtained from the stellar population synthesis code STARBURST99 (Leitherer al. 1999), with an upper mass limit of 100 M$_\odot$ and an age of 1 Myr. For the hypothetical nebula, we adopted a constant electron density N_e = 200 cm^{-3}, a plane-parallel geometry and a solar abundance ratio log(Ne/O) = -0.61 (oxygen from Allende Prieto, Lambert & Asplund 2001 and Ne from Grevesse & Sauval 1998). In the models with Z = 2 Z$_\odot$, a value of log(Ne/O) = -1.0 was assumed, in order to fit the data in this high-metallicity regime. This value is about the same as that found by Pérez-Montero et al. (2007) for very high metallicities. A complete description of the photoionization models has been presented by Dors et al. (2011).

Fig. 3 shows the diagnostic diagrams containing the observed emission-line intensities and the photoionization model results. The typical errors of the observational emission-line ratios are about 10 per cent. It can be seen that the majority of the observational data fall within the regions occupied by the models when all the considered emission lines are in the optical range (see both upper panels and the lower-left panel). However, in lower-right panel of Fig. 3, it can be seen that the models produce lower values of the intensity line ratio [Ne III]15.56 μm/[Ne II]12.81 μm. This problem was pointed out by Pérez-Montero & Vílchez (2009) and Morisset et al. (2004), who found similar results from photoionization model grids built assuming different atmosphere models as photoionization sources. They concluded that this effect could not be the result of uncertainties in stellar atmosphere models and must be because of problems in the atomic data of the mid-IR lines.

4 DETERMINATION OF IONIC ABUNDANCES

We have considered two methods to determine the Ne^{++}, Ne$^+$, O$^+$ and O^{++} ionic abundances in our sample: the method that uses direct estimations of the electron temperatures (which we call the visible-lines method) and the method that uses IR emission lines (which we call the IR-lines method).
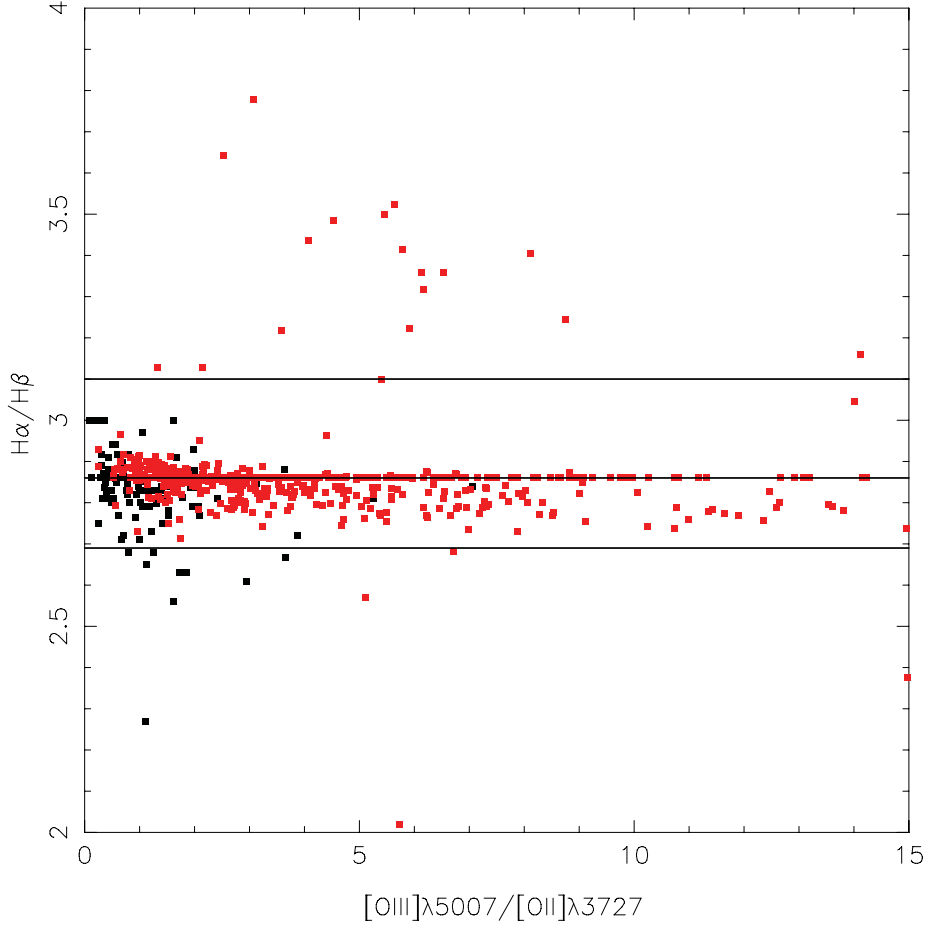
Figure 2. Hα/Hβ versus [O III]λ5007/[O III]λ3727. The black and red squares represent the H II regions and ELGs, respectively, compiled from the literature. All data were reddening corrected in the works from which we have taken the data. The lines represent the theoretical values for the low-density recombination case B Balmer decrement Hα/Hβ = 3.10, 2.86 and 2.69 for temperatures of 5000, 10 000 and 20 000 K, respectively (Osterbrock 1989; Storey & Hummer 1995).

4.1 Visible-lines method

For those objects with the appropriate optical emission-line measurements, we calculated the electron temperature (T_e) from the observed line-intensity ratio $R_{O3} = $ [O III]($\lambda4959 + \lambda5007$)/$\lambda4363$ for the high-ionization zone (referred to as t_3). To do this, we used the fitting function derived by Hägele et al. (2008) based on the TEMDEN routine of the nebular package of the IRAF:[1]

$$t_3 = 0.8254 - 0.0002415 R_{O3} + \frac{47.77}{R_{O3}}. \qquad (1)$$

Here, t is in units of 10^4 K. The electron density (N_e) was computed from the ratio of [S II]λ6716/λ6731 using the TEMDEN routine and t_3 values given by equation (1).

The O^{++} and Ne^{++} abundances were computed using t_3 and following the relations given by Pérez-Montero et al. (2007):

$$12 + \log\left(\frac{O^{++}}{H^+}\right) = \log\left[\frac{I(4959) + I(5007)}{I(H\beta)}\right] + 6.144$$
$$+ \frac{1.251}{t_3} - 0.55 \log t_3; \qquad (2)$$

$$12 + \log\left(\frac{Ne^{++}}{H^+}\right) = \log\left[\frac{I(3869)}{I(H\beta)}\right] + 6.486$$
$$+ \frac{1.558}{t_3} - 0.504 \log t_3. \qquad (3)$$

The O^+ ionic abundances were computed assuming $N_e = 100$ cm^{-3} and an electron temperature of the low-ionization zone (referred to as t_2) derived from the theoretical relation

$$t_2^{-1} = 0.693\, t_3^{-1} + 0.281, \qquad (4)$$

which was obtained from the models described by Pérez-Montero & Díaz (2003). Measurements of the [O II]λ7325 auroral emission line, sensitive to the [O II] electron temperature, are available for only 10–15 per cent of our sample. Because we use the observational sample in a statistical way, we prefer to derive all the temperatures following the same procedure. Besides, almost all the objects present high or moderate excitation degrees: (I[O III]λ4959+λ5007)/(I[O II]λ3727+ I[O III]λ4959+λ5007) $\geq$ 0.4, as defined by Pilyugin (2001). Therefore, the impact of the O^+/H^+ variations on the total oxygen abundance and on the $O^{++}/(O^{++} + O^+)$ ratio (used in the neon ICF determinations) is small ($\approx$18 per cent) and, from a statistical point of view, negligible. It is only in those cases where
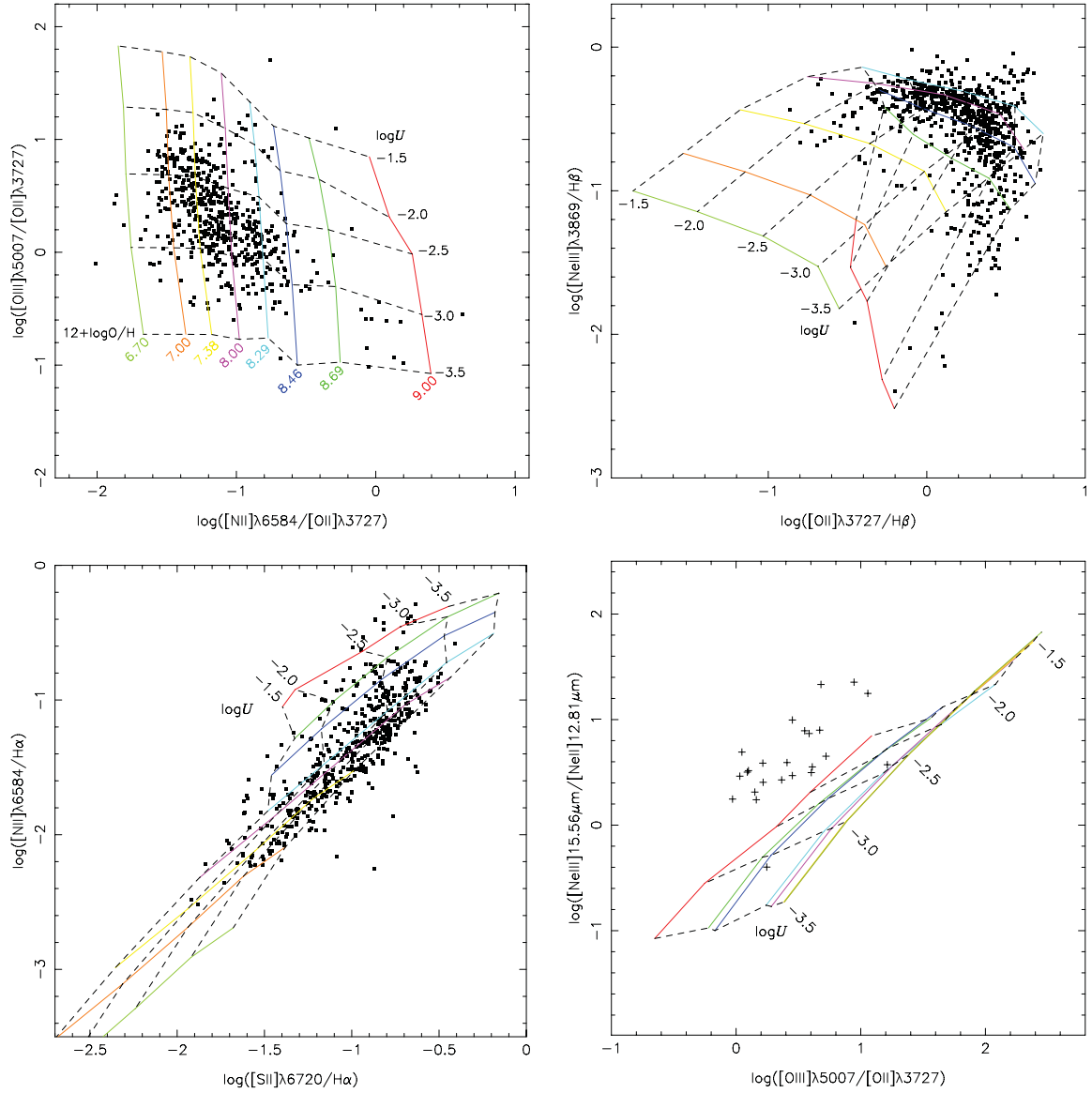
Figure 3. Diagnostic diagrams containing observational data taken from the literature (all groups) and the results of the grid of photoionization models described in this work. The solid lines connect the curves of iso-(O/H), while the dashed lines connect the curves of iso-U. The colour code for the values of the oxygen abundances (tracer of the metallicity) is the same in all panels and is indicated in the upper-left panel. The solar oxygen abundance refers to Allende Prieto et al. (2001) and corresponds to $12+\log(\text{O/H}) = 8.69$. The values of $\log U$ are indicated in each panel. The points are the observational data. The typical errors (bars not shown) of the observational emission-line ratio are about 10 per cent.

the [O III]λ4363 and [O II]λ7325 auroral emission lines were not available that we have computed the O^+ ionic abundances, assuming the electron temperature directly estimated from the observed line-intensity ratio $R_{N2} = [\text{N II}](\lambda6548 + \lambda6584)/\lambda5755$:

$$t_2 = 0.537 - 0.000253R_{N2} + \frac{42.13}{R_{N2}} \qquad (5)$$

fitting function taken from Hägele et al. (2008). For a few objects (<1 per cent), t_2 was derived using this equation.

To derive the O^+ ionic abundances, we used the expression given by Hägele et al.:

$$12 + \log\left(\frac{\text{O}^+}{\text{H}^+}\right) = \log\left[\frac{I(3727)}{I(\text{H}\beta)}\right] + 5.992 + \frac{1.583}{t_2}$$
$$- 0.681 \log t_2 + \log(1 + 2.3n_e). \qquad (6)$$

Here, $n_e = N_e/(10^4\,\text{cm}^{-3})$. As pointed out by Hägele et al., the expressions given above are valid for temperatures from 7000 to 23 000 K. The O^+ ionic abundances, calculated using the t_2 values from equations (4) and (5), differ by about 0.2 dex. The data set used to determine the ionic abundances with this method belongs to groups A and B and is comprised of 579 objects ($\sim$80 per cent of the sample). All O^+, O^{++} and Ne^{++} ionic abundances obtained with the visible-lines method used in this study have been computed from this data set.

4.2 Infrared-lines method

The Ne^+ and Ne^{++} ionic fractions can be determined using the intensities of the [Ne II]12.81 μm and [Ne III]15.56 μm emission lines, respectively, and following a similar methodology to the one

presented by Förster et al. (2001). The ionic abundance of an element can be given by

$$\frac{n_{X^{+i}}}{n_{H^+}} = \frac{I_\lambda(X^{+i})N_e\, j_{\lambda(H^+)}}{I_\lambda(H^+)N_e\, j_{\lambda(X^{+i})}}. \tag{7}$$

Here, $n_{X^{+i}}$ and n_{H^+} are the densities of the ions X^{+i} and H^+, $I_\lambda(X^{+i})$ is the intensity of a given emission line emitted by X^{+i}, $I_{\lambda(H^+)}$ is the intensity of a reference hydrogen line, while $j_{\lambda(X^{+i})}$ and $j_{\lambda(H^+)}$ are the emissivity values given by the IONIC routine of the nebular package of IRAF, which uses the Ne atomic parameters from Badnell et al. (2006), Griffin, Mitnik & Badnell (2001), Kaufman & Sugar (1986), Butler & Zeippen (1994) and Mendoza (1983). These emissivity values are assumed to be constant in all abundance determinations because these vary by less than 5 per cent over a large temperature range (see the pioneering work by Simpson 1975).

Using this method, any error in the determination of these emissivities directly translates in a systematic shift in the derived Ne^+ and Ne^{++} ionic abundances. Taking into account all these assumptions, we obtain

$$\frac{Ne^+}{H^+} = \frac{I(12.81\,\mu m)}{I(H\beta)} \times 1.322 \times 10^{-4} \tag{8}$$

and

$$\frac{Ne^{++}}{H^+} = \frac{I(15.56\,\mu m)}{I(H\beta)} \times 6.323 \times 10^{-5}. \tag{9}$$

5 COMPARISON OF NEON IONIC DETERMINATIONS

With the aim of comparing the Ne^{++}/H^+ ionic abundances derived using the visible-lines method with those derived using the IR-lines method, in Fig. 4 we plot the results for the 23 objects listed in Table 2. These are the only objects for which we are able to apply both methods. These objects simultaneously belong to either group A or B, and to group E. We can see a large discrepancy and scatter. Comparing the Ne^{++}/H^+ ionic abundance determinations obtained using the visible-lines method with those based on the IR-lines method, we find discrepancies of about a factor of 4, on average, with Ne^{++}/H^+ being underestimated when using the visible-lines method (see Fig. 4).

The origin of this discrepancy is uncertain and several explanations have been proposed. Vermeij & van der Hulst (2002) have compared the optical and IR ionic fractions obtained for a sample of H II regions located in the Magellanic Clouds. They found considerable discrepancies between the determinations found using these two methods, which were attributed to the difference in the area of the sky covered by the IR and optical observations. However, as discussed above, aperture effects are probably not the origin of this huge discrepancy regarding a high-excitation ion such as Ne^{++}.

Extinction might noticeably affect the comparison between the abundances obtained from IR and optical emission lines. The blue optical [Ne III] emission line is more absorbed by dust than the mid-IR lines. Hence, if the nebular emission is highly reddened by dust, the optical line does not trace all the Ne in the inner parts of the star-forming regions, yielding an optical ionic abundance lower than that derived from the mid-IR lines. In the same way as for the Ne emission lines, this effect could be enhanced by the use of $H\beta$ or $Br\beta$ emission lines, instead of $Hu\alpha$, to derive ionic abundances in the mid-IR. In order to verify the extinction influence on the emission lines, models with different internal dust abundance were built. In these, only the effect of grains on the continuous opacity was
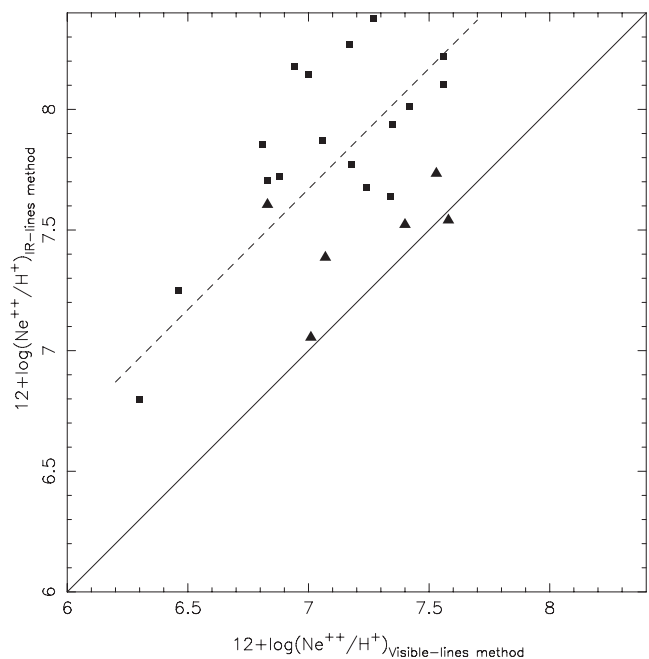

Figure 4. Comparison between the ionic abundance of Ne^{++}/H^+ derived using the visible-lines and IR-lines methods. The points represent estimations for the objects presented in Table 2, where squares and triangles are the estimations made using $H\beta$ and $Br\beta$ fluxes, respectively. The solid line represents the equality of the two estimates. The dashed line is the equality line shifted by the average of the differences between the ionic abundances. Typical errors in optical and IR estimations are about 15 and 10 per cent, respectively (Vermeij & van der Hulst 2002).

considered (i.e. the gas heating by grain emission was not considered in the calculations). The dust abundance was linearly scaled with the default value assumed in the CLOUDY code (i.e. $\log O/H \approx -4$). The grain model has been described by van Hoof et al. (2001). Fig. 5 shows the predicted luminosity values ($L/L_{\text{free dust}}$) for some hydrogen and neon emission lines in relation to the ones predicted by the model that is free of dust ($Z_{\text{dust}}/Z_{\text{van Hoof}} = 0$). We can see that $H\beta$, $Br\beta$ and $Hu\alpha$ have about the same decrease with the dust abundance, reaching a ~ 4 per cent maximum difference in their luminosities for $Z_{\text{dust}}/Z_{\text{van Hoof}} = 10$. A similar behaviour is found for the neon emission lines, with a difference of about 6 per cent. Even though these differences are within the observational measurement errors, we have used these predicted emission-line intensities to calculate the Ne^{++} abundance following the same procedure as presented in Section 4. The largest difference found in the Ne^{++} abundances, derived from the IR-lines and the visible-lines methods, is 0.3 dex. Therefore, this result shows that, at least, the extinction caused by the internal dust is not the main source of the neon ionic discrepancy.

To verify if there is an observational correlation between the extinction and the abundance discrepancy for the 23 objects listed in Table 2, in Fig. 6 we plot the difference (D) between the Ne^{++} ionic abundances obtained using the IR-lines and visible-lines methods versus the nebular reddening constant [$C(H\beta)$], which is compiled from the literature, and has been used by the authors to correct their observational data. There is no evident correlation between the discrepancy and the extinction found from the Balmer decrement.

For five objects of our sample (i.e. N81, N4A, N66, N160A1 and N160A2), both $Br\beta$ and $H\beta$ fluxes were obtained directly from spectroscopy observations by Vermeij et al. (2002), Dufour &
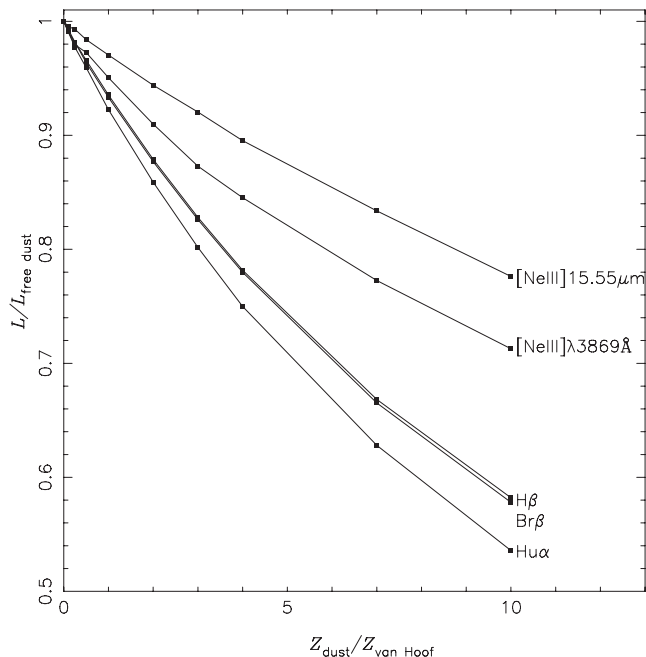
Figure 5. Logarithm of the luminosity predicted by our models for some hydrogen and neon emission lines versus the dust internal abundance, in relation to the default value assumed in the CLOUDY code (i.e. $\log O/H \approx -4$). The grain model has been described by van Hoof et al. (2001). The points are the results for models considering different dust abundances connected by the curves. The results for different emission lines are indicated. Here, $Z_{dust}/Z_{van\ Hoof} = 0$ represents the models free of internal dust.
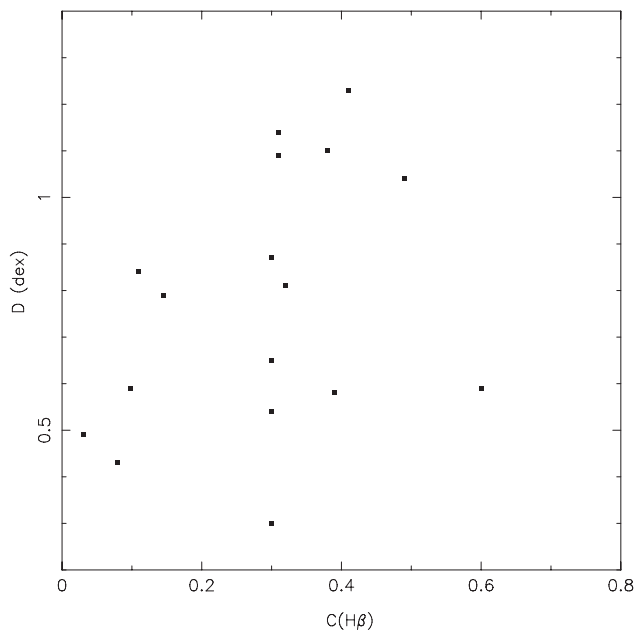
Figure 6. Differences between Ne^{++} ionic abundances obtained using the IR-lines and visible-lines methods, as a function of the nebular reddening constant $C(H\beta)$ for the majority of the objects listed in Table 2.

Harlow (1977a,b), Heydari-Malayeri, Le Bertre & Magain (1998) and Heydari-Malayeri et al. (2002). We have used these data, and [Ne III]15.55 μm from Vermeij et al. (2002), to calculate the Ne^{++}/H^+ ionic abundances of these objects, using both hydrogen lines. We have found neon ionic estimations in agreement by about 0.2 dex, indicating that dust absorption is not the main source of the

discrepancy, at least for these objects. Further observational support for this result arises from the data presented by Wu et al. (2008), who have pointed out that most of the galaxies that they have observed, which include 50 per cent of the ELGs presented in Table 2, do not show a strong 9.7-μm silicate feature, and consequently have low dust extinction. Moreover, as noted in Fig. 4, for the objects where both $Br\beta$ and $H\beta$ fluxes have been measured, the ionic difference is also found, indicating that the differential absorption of optical and IR emission lines is not the main cause of the discrepancy. Thus, we can assume that this effect is negligible for these objects.

As can be seen in Section 3, and has already been noted by Pérez-Montero & Vílchez (2009) and Morisset et al. (2004), the photoionization models cannot reproduce diagnostic diagrams based on Ne mid-IR lines, independently of the stellar atmospheres used. Therefore, this could be symptomatic of inaccurate atomic data involving these emission lines and can be on the basis of the discrepancies found when deriving abundances from optical and mid-IR emission lines. In particular, the atomic parameter that can affect the abundance determinations is the collision strength for the [Ne III]λ15.56 μm emission line. However, it is not probable that the uncertainties in this parameter are the main cause of the discrepancy found in our study. Over the years, differences in the neon collision strength have been found. For example, the collision strength for [Ne III] $^3P_1 \rightarrow {}^3P_2$ derived by Blaha (1969) is $\Omega = 0.581$. The Ω values derived in the IRON project by Butler & Zeippen (1994) range from 0.481 to 0.778 for temperatures ranging from 10^3 to 10^5 K. Later computations by McLaughlin & Bell (2000) yielded a value of Ω lower by about 20 per cent than the value proposed by Blaha (1969). Recently, McLaughlin et al. (2011) have recomputed the collision strengths for some neon lines using a small-scale 56-level Breit–Pauli calculation and a large-scale 554-level R-matrix intermediate coupling frame transformation (ICFT). They have shown that different values of Ω are obtained by the use of these suppositions, in the sense that for the 56-level Breit–Pauli calculation Ω ranges from about 0.5 to 1.0 and for the 554-level ICFT it ranges from about 0.4 to 0.8. It must be noted that these results are in good agreement with earlier derivations. Nevertheless, even assuming that the collision strength for the [Ne III]λ15.56 μm emission line can vary by a factor of 2, it is not enough to conciliate the ionic abundance discrepancy.

Finally, another supposition is the presence of electron temperature fluctuation amplitude inside the ionized gas. This can lead to an underestimation of the ionic abundances obtained via optical collisionally excited lines when these fluctuations are not considered, because these lines are strongly dependent on the electron temperature (e.g. Peimbert 1967, 2003; Krabbe & Copetti 2005). This problem can be alleviated using abundances based on IR emission lines, whose fine-structure transitions have a weak dependence on the electron temperature (e.g. Dinerstein, Lester & Werner 1985; Rubin et al. 2001; Nollenberg et al. 2002; Garnett et al. 2004). Because the electron temperatures are related to the chemical composition of the emitting gas, temperature fluctuations are essentially equivalent to abundance variations across the nebula (Kingdon & Ferland 1998).

To test the effect of the presence of temperature fluctuations and/or abundance variations, we built a grid of photoionization models using CLOUDY. These models are similar to the models described in Section 3 and presented in Fig. 3, but considering the presence of chemical inhomogeneities in the theoretical nebula and spherical geometry. The plane-parallel geometry assumed in the models described in Section 3 cannot be used to test variations along the radius of the hypothetical nebulae, because this makes
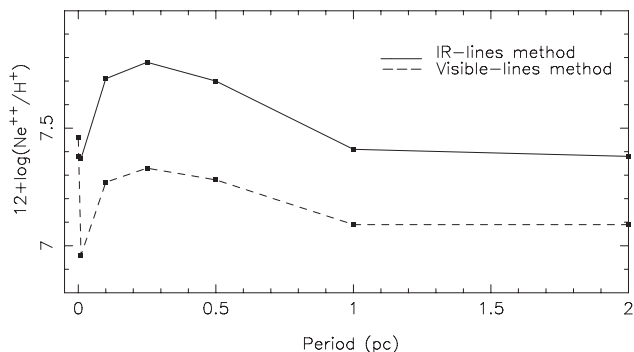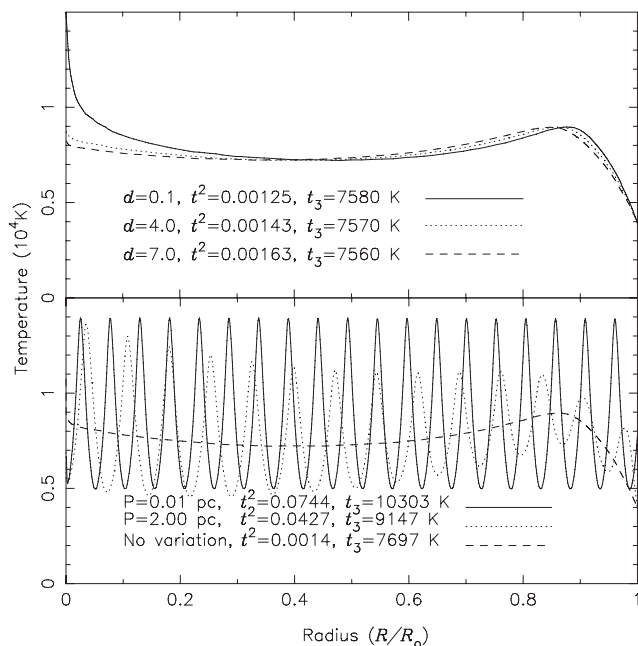
Figure 7. Results of photoionization models considering abundance variations along the radius of the nebula. The Ne^{++}/H^+ ionic abundances are obtained using the visible-lines and IR-lines methods (dashed and solid lines, respectively) as a function of the period P of the abundance variations.

the inner radius much larger than the thickness of the cloud and the results about independent on electron temperature fluctuation amplitude. In this case, we have considered a nebula with $Z = Z_\odot$, with an inner radius of 4 pc and an outer radius where the temperature falls below 4000 K ($\approx$30 pc), and a number of hydrogen-ionizing photons emitted by the ionizing star cluster of 10^{50} s^{-1}. It was assumed that the metallicity varies along the radius of the nebula as a sine wave, with period P ranging from 0.01 to 2 pc, including 0.01, 0.1, 0.25, 0.5 and 1 pc. Also, a model with no variations and solar abundance was considered. We have considered a set of models with an abundance amplitude of 0.8 dex, which takes metallicity values between $2 \times Z_\odot$ and $0.3 \times Z_\odot$. Kingdon & Ferland (1995) built grids of photoionization models using similar sine wave variations but applied to the total hydrogen density across the nebula.

We have used the emission-line intensities given by our models for each value of P to calculate the Ne^{++}/H^+ ionic abundances. We have applied the visible-lines and IR-lines methods, following the same procedure as described in Section 4. Thus, we obtain two estimations of Ne^{++}/H^+ for each model. Fig. 7 shows these estimated values of Ne^{++}/H^+ plotted as a function of the period P of the abundance variations. As can be seen when no variations are considered, the Ne^{++}/H^+ ionic abundances estimated by each method differ by less than 0.1 dex, which is within the errors of the methods. When abundance variations are present, the differences could reach about 0.5 dex, with the ionic abundances obtained with the IR-lines method being largest. This value is very similar to the value found in Fig. 4 between the estimated Ne ionic abundances derived by applying the visible-lines and IR-lines methods to the observational data. Moreover, these differences, as expected, depend on the metallicity amplitude of the models, increasing (decreasing) with an increment (decrement) in the amplitude (models not shown). Therefore, the temperature fluctuations studied through the abundance variations across the nebula could be a possible explanation for the discrepancy between the estimated Ne abundances by these two methods. In Fig. 8 (bottom panel), we have plotted the temperature structure[2] of our models with $P = 2$ and 0.01 pc, and no fluctuations versus the radius normalized to the outermost radius. In this figure, we also show, for each P, the values of the temperature fluctuation parameter (t^2), as defined by Peimbert (1967), and

---

[2] In the CLOUDY code, the nebula is divided into concentric zones, with the physical conditions across them about constant. This causes the zone number in each computed model to vary. The electron temperatures of these zones are shown in Fig. 8. See the CLOUDY manual for more details.

Figure 8. Temperature structure of the theoretical nebula from our photoionization models. For each model, R/R_o is the radius normalized to the outermost radius (R_o). In the bottom panel, the curves represent the results of models with different values of P (i.e. the period of the sine wave in which the metallicity varies along the radius of the nebula), as indicated. In the top panel, the curves represent the results of models with no abundance variations but with different distances between the central ionizing source and the inner face of the gas, represented by d, as indicated. We show t^2, as defined by Peimbert (1967), and the electron temperature t_3 for each of the models.

the electron temperature t_3, using the predicted values of R_{O3} and equation (1).

As expected, we have found that abundance variations translate into temperature fluctuations. As can be seen in Fig. 8, t_3 decreases when larger values of P are assumed. However, the average temperature weighted by the electron density over the volume of the nebula $\langle T \rangle$ (not shown), as defined by Peimbert (1967), is about constant with P. The model with $P = 0.01$ pc shows a constant temperature fluctuation amplitude of about 9000 K, while the amplitude shown by the model with $P = 2$ pc decreases with the radius. Interestingly, when no fluctuations are considered, the t^2 value is about the same found as that in some H II regions (e.g. Krabbe & Copetti 2002) and H II galaxies (e.g. Hägele et al. 2006). However, the t^2 values that explain the differences found when comparing ionic abundances obtained via recombination and collisional excited emission lines (e.g. Peimbert 2003; García-Rojas et al. 2006) are in good agreement with those given by the models with P different from zero. Copetti (2006) have carried out a more detailed study of spatial electron temperature fluctuations in ionized nebulae from photoionization models.

Over several decades, observations have failed to find direct evidence of chemical inhomogeneities in H II regions (e.g. Krabbe & Copetti 2002; García-Rojas et al. 2006; Lebouteiller et al. 2008; Oliveira, Copetti & Krabbe 2008) and in planetary nebulae (e.g. Liu et al. 2000; Rubin, Bhatt & Dufour 2002; Krabbe & Copetti 2005). Thus, another source of temperature fluctuations could be the presence of density variations in the gas. Rubin (1989) has shown that large-scale variations in electron density in the gas do cause electron temperature fluctuations. Consider the H II region models

of Rubin (1985), who pointed out that if N_e varies by a factor of about 10, the electron temperature can range up to 2000 K (see also Kingdon & Ferland 1995). Recently, Mesa-Delgado et al. (2012) have presented results from the integral field spectroscopy of a region near to the Trapezium Cluster. They found the presence of high-density gas ($N_e \approx 4 \times 10^5\,\mathrm{cm}^{-3}$), with values much higher than the typical values obtained for either galactic or extragalactic regions (see Copetti et al. 2000). Unfortunately, a larger number of observations, such as those by Mesa-Delgado et al. (2012), are needed to confirm the high-scale density fluctuations in ionized nebulae.

Another likely reason for the presence temperature fluctuations is different proximities of gas to the ionizing O stars, because these are mainly responsible for the ionization structure. To test this, we have built models considering different distances, d, between the central ionizing source and the inner face of the gas, where d ranged from 0.1 to 7 pc. These values are consistent with the values used by Simpson et al. (1997) in a study of the Galactic H II region G0.18–0.04. Again, the predicted emission lines were used to calculate the Ne^{++}/H^+ ionic abundances, by applying the visible-lines and IR-lines methods, following the same procedure as described in Section 4. We found a 0.0–0.2 dex difference in Ne^{++}/H^+. Fig. 8 (top panel) shows the temperature structure of the models. We can see a hot region very near to the central star, but this region is too small to affect the derived abundances; we do not obtain any significant changes in the models in either the t^2 or t_3 values. Models with a more complicated geometry, with many stars distributed through the gas (e.g. Ercolano, Bastian & Stasińska 2007), might cause temperature variations, and consequently might help to explain the Ne^{++}/H^+ ionic discrepancies.

6 NEON IONIZATION CORRECTION FACTORS

6.1 Determinations of ionization correction factors

The ICFs represent the unseen ionization stages of each element. For Ne^{++}, the ICF is defined as

$$\mathrm{ICF}(Ne^{++}) = Ne/Ne^{++}. \tag{10}$$

The ICF for Ne^{++} can be directly computed using only [Ne II]12.81 μm and [Ne III]15.56 μm emission-line fluxes. Assuming that the total Ne abundance is

$$\frac{Ne}{H} \approx \frac{Ne^+}{H^+} + \frac{Ne^{++}}{H^+}, \tag{11}$$

and using equation (10), we have obtained

$$\mathrm{ICF}(Ne^{++}) = 1 + \frac{Ne^+}{Ne^{++}}. \tag{12}$$

Using equations (8) and (9), we have found

$$\mathrm{ICF}(Ne^{++}) = 1 + 2.10 \times \frac{F_{[Ne\,II]\lambda12.81\,\mu m}}{F_{[Ne\,III]\lambda15.56\,\mu m}}. \tag{13}$$

Therefore, to estimate the Ne ICF using the IR lines, it is not necessary to use hydrogen emission-line fluxes. Thus, we have been able to use all the objects belonging to group E (143 objects). Fig. 9 shows a histogram containing the ICF values lower than 10. It can be seen that almost all the ICF values ($\approx$85 per cent) are lower than 5. Very high values (>10) are also found. The objects that present the largest ICF values are IC 342 ($\approx$257), NGC 5236 and 5253 ($\approx$58), Searle 5 ($\approx$55), NGC 3628 ($\approx$45) and NGC 2903 ($\approx$32). Also, high
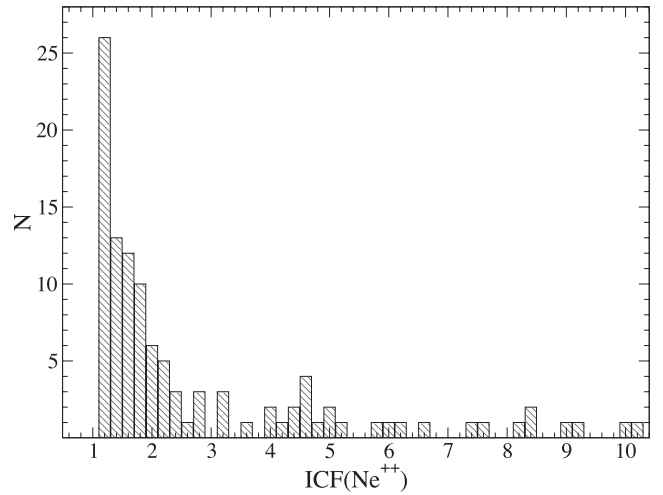
Figure 9. Histogram containing the values of the ICF(Ne^{++}) obtained using the IR emission-line intensities and equation (13) for the objects belonging to group E and with ICF values lower than 10.

ICFs have been obtained from the data of some H II regions in M83, observed by Rubin et al. (2007). These values (not shown) could reflect the presence of cool ionizing sources in these objects.

A classical way to determine the neon ICF takes advantage of its relation with the ionic oxygen $O^{++}/(O^+ + O^{++})$ ratio. From a fit in our photoionized model results presented in Section 3, we have obtained

$$\mathrm{ICF}(Ne^{++})_{\mathrm{model}} = 0.741 - 0.08x + \frac{0.393}{x}, \tag{14}$$

where $x = O^{++}/(O^+ + O^{++})$. This relation is shown in Fig. 10. This figure also shows the ICFs obtained using the photoionization models of Pérez-Montero et al. (2007) and Izotov et al. (2006a), the
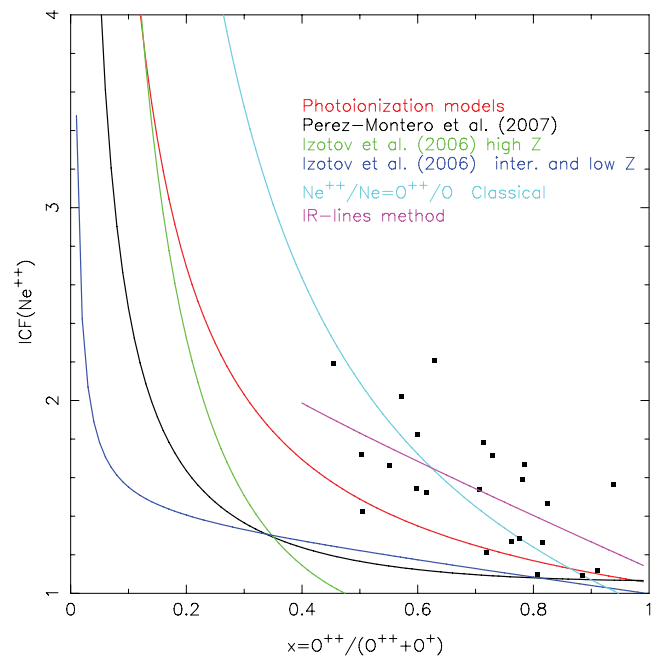
Figure 10. Relation between ICF(Ne^{++}) and $x = O^{++}/(O^+ + O^{++})$ ionic abundance ratio. Solid lines correspond to our fits to the ICF for Ne and those found by other authors, as indicated. Points represent the data where the ICFs were determined via the IR-lines method, as listed in Table 2.

classical approximation [ICF(Ne^{++}) = O/O^{++}] – where the ionic abundances are derived both from the visible-lines method and using our data sample – and the ICFs obtained from the IR-lines method.

Fitting the results from using the ICF obtained with the IR-lines method and using x obtained with the visible-lines method, represented by points in Fig. 10, we obtain

$$\text{ICF(Ne}^{++})_{\text{IR}} = 2.382 - 1.301x + \frac{0.05}{x}, \qquad (15)$$

valid for $x \geq 0.4$. Unfortunately, we only have measurements of the Ne IR emission-line intensities for 23 objects in our sample, and we have determined the O^{++}/(O$^+$ + O^{++}) ratio via the visible-lines method (see Fig. 10). It must be noted that this sample comprises objects in a large range of metallicity ($7.1 < 12 + \log(\text{O/H}) <$

8.50 dex) as well as a large range of ionization degree ($0.4 < $ O^{++}/(O$^+$ + O^{++}) < 1.0).

6.2 Application of the neon ionization correction factors

To test the differences in the Ne/H total abundance yielded by the use of different ICFs, we have used the observational data to compute Ne^{++}/H$^+$ ionic abundances with the visible-lines method, and we have applied different ICFs to obtain the Ne total abundances. Fig. 11 shows the comparisons between the Ne/H derived using the ICF from the IR-lines method (equation 15) and those values estimated by applying the ICFs derived by Pérez-Montero et al. (2007) (see Fig. 11a), Izotov et al. (2006a) (see Fig. 11b), the photoionization models (equation 14) described in this work (see Fig. 11c) and the classical approximation, ICF(Ne^{++}) = O/O^{++} (see Fig. 11d).
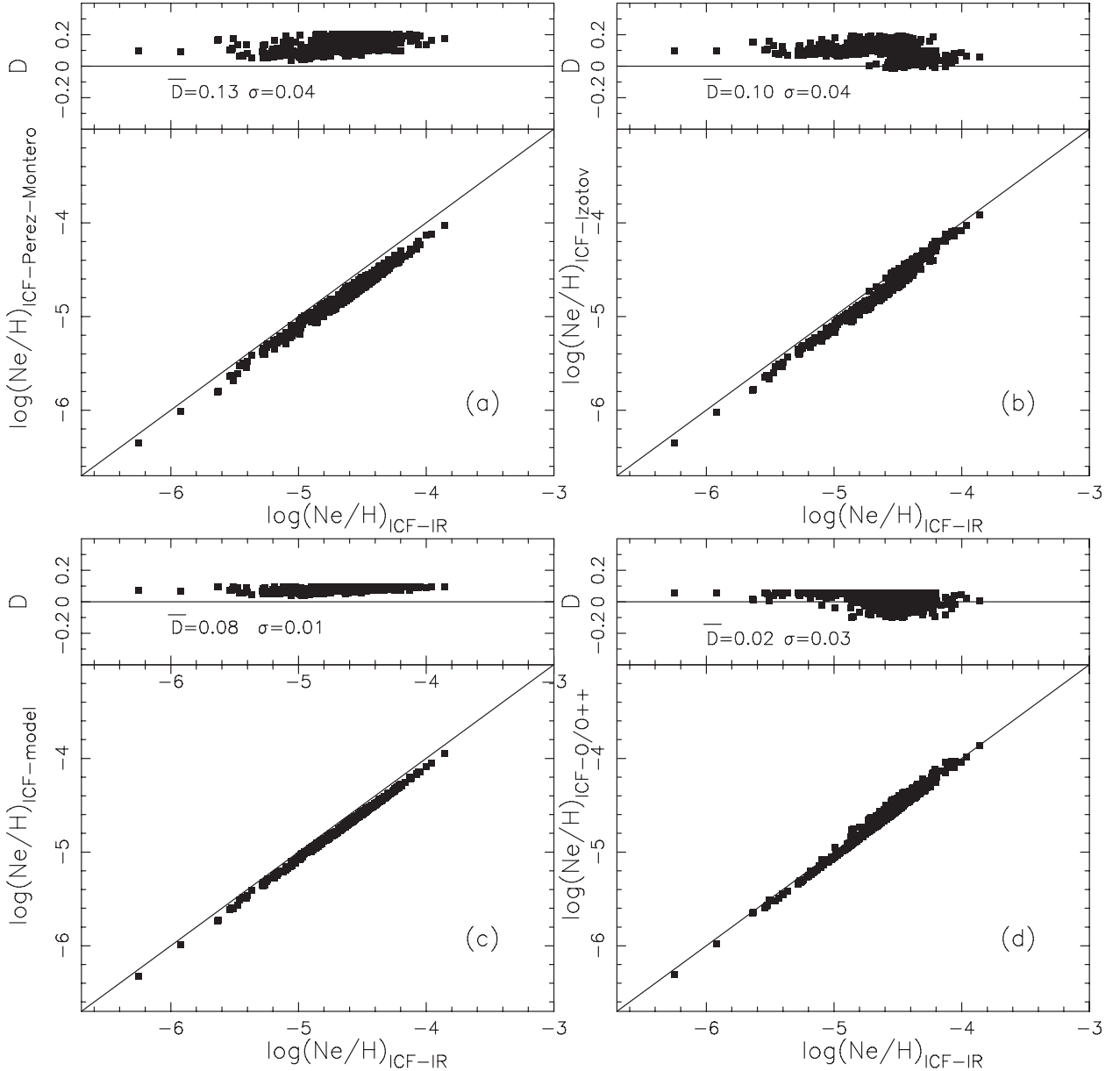
Figure 11. Comparison between the total Ne/H abundances obtained from the Ne^{++}/H$^+$ ionic abundances using the visible-lines method and by applying different ICFs, as indicated. Points represent estimations for the objects belonging to groups A and B. The top panel of each diagram shows the difference between the estimations using the methods considered. The average value $\overline{D}$ of this difference and the dispersion are shown in each plot. Solid lines represent the equality of the two estimates.
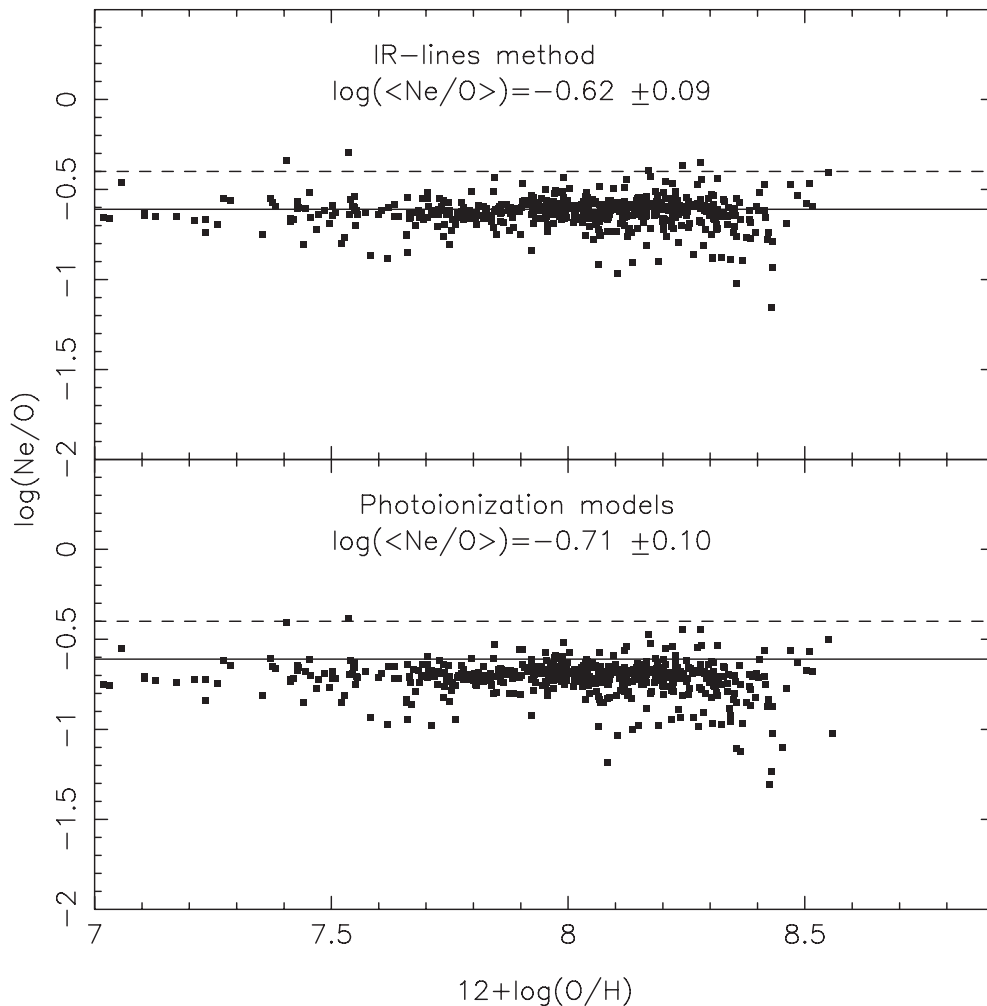
Figure 12. Relation between log(Ne/O) and O/H using the visible-lines method and our two different ICF(Ne^{++}), as indicated. Points represent estimations for the objects belonging to groups A and B. The solid line represents the Ne/O abundance ratio derived using the oxygen abundance from Allende Prieto et al. (2001) and neon from Grevesse & Sauval (1998), while the dashed line represents the value derived by Drake & Testa (2005) using the *Chandra* X-ray spectra of a sample of nearby solar-like stars. The average and the standard deviation of log(Ne/O), taking into account low- and high-metallicity regimes, are shown in each plot.

It can be seen that, in general, the expression from the IR-lines method gives higher ICF values, and consequently higher Ne/H values, by about 0.08–0.13 dex, than those obtained using the ICFs from Pérez-Montero et al. (2007), from Izotov et al. (2006a) and from our photoionization models. For low-excitation objects, we find that the high-metallicity models of Izotov et al. (2006a) are in agreement with our theoretical relation. Finally, the classical ICF approximation yields Ne/H values in agreement with the ICFs obtained with the IR-lines method.

6.3 Ne/O versus O/H

A very important issue is the study of the relation between the Ne/O ratio and the total oxygen abundance, for which there is not yet a consensus. Using the oxygen and neon abundances of a sample of planetary nebulae and H II regions, Wang & Liu (2008) have found that the Ne/O ratio increases with O/H in both types of nebulae. A similar result was found by Guseva et al. (2011) and Izotov et al. (2006a) for a large sample of low-metallicity ELGs. For a large sample of star-forming regions, using a photoionization model grid to derive the Ne ICF, Pérez-Montero et al. (2007) have found that

the Ne/O behaviour agrees with the assumption of a constant value for the low-metallicity regime [12+log(O/H) < 8.2] but shows a slight decrease for the high-metallicity regime [12+log(O/H) > 8.2]. Moreover, using the mid-IR derivations of the neon abundances of a sample of H II regions located in M33, Willner & Nelson-Patel (2002) have obtained a flat neon abundance gradient as a function of the galactocentric radius, as well as a decrement of the Ne/O ratio when O/H increases.

To investigate this issue, we have applied the different ICFs for Ne, shown in Fig. 10, to the ionic Ne^{++} abundances estimated using the visible-lines method, in order to obtain the total Ne abundances for the compiled sample. We have combined these values with the total oxygen abundances to estimate the Ne/O ratio. Figs 12 and 13 show these values as a function of 12+log(O/H) for our ICFs and for those from the literature, respectively. In these figures, we also show the logarithm of the average Ne/O value derived using the different ICFs, and their standard deviations. These average values are consistent in all cases with the adopted solar value. From a visual inspection of the distributions of our observational sample in these diagrams, it can be seen that there is a flat relation between the logarithms of the Ne/O and O/H ratios for the whole metallicity
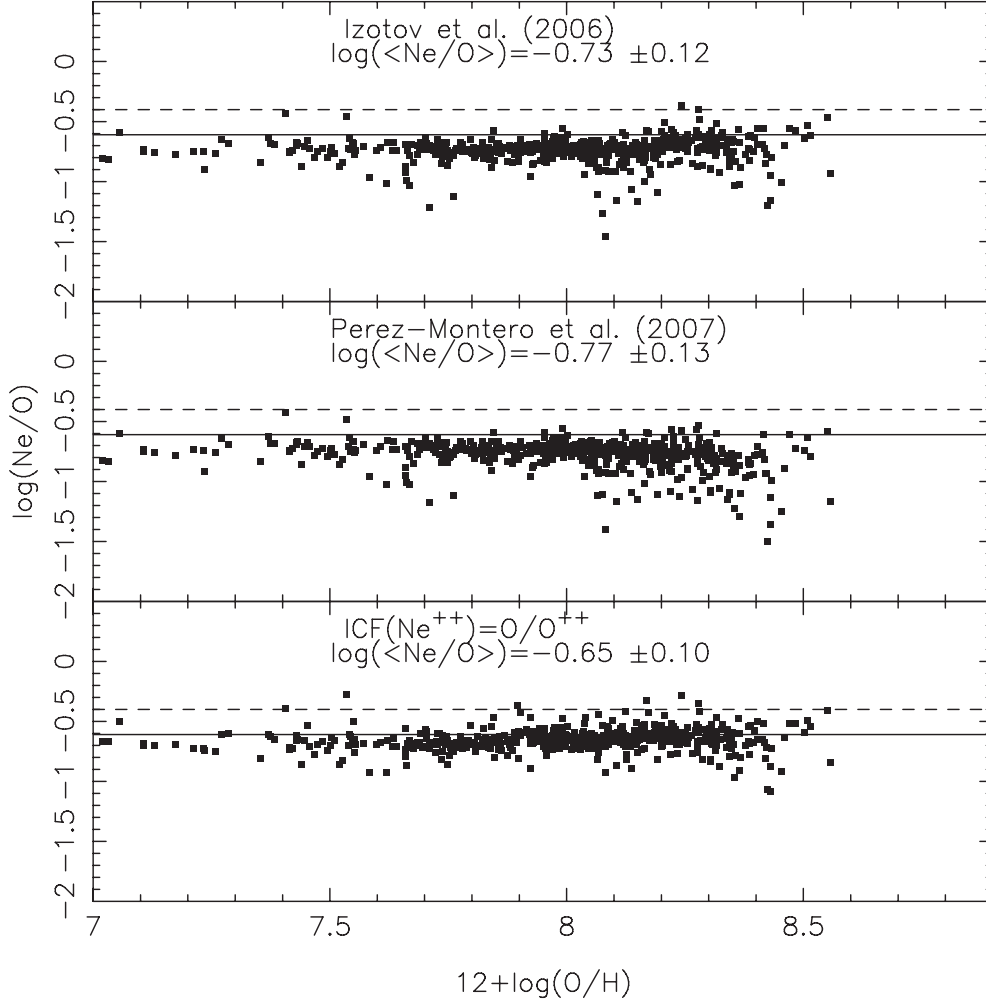
Figure 13. As Fig. 12, but for the ICF(Ne^{++}) from the literature, as indicated.

Table 3. Coefficients of the linear regressions log(Ne/O) = a × [12+log(O/H)] + b fitted to the data plotted in Figs 12 and 13. Columns 2 and 3 list the slope and the constant coefficient, respectively, together with their formal errors. Columns 4 and 5 are the mean values of log(Ne/O) for the high- and low-metallicity regimes considered.

			log($\langle$Ne/O$\rangle$)	
ICF(Ne^{++})	a	b	High Z	Low Z
IR-lines method	$+0.02 \pm 0.01$	-0.77 ± 0.11	-0.63 ± 0.11	-0.62 ± 0.08
Photoionization models	-0.02 ± 0.01	-0.53 ± 0.10	-0.74 ± 0.13	-0.70 ± 0.09
Izotov et al. (2006a)	$+0.06 \pm 0.01$	-1.17 ± 0.12	-0.70 ± 0.12	-0.75 ± 0.10
Pérez-Montero et al. (2007)	-0.08 ± 0.01	-0.08 ± 0.14	-0.83 ± 0.13	-0.75 ± 0.13
ICF(Ne^{++}) = O/O^{++}	$+0.04 \pm 0.01$	-1.06 ± 0.12	-0.64 ± 0.11	-0.65 ± 0.09

range studied, from about 7 to 8.5 dex. We have also performed a fit to these data, assuming a linear regression with slope a and the regression constant b, and without taking into account the individual errors. In Table 3, we list the coefficients of the fittings. We obtain null, positive and negative slopes for the different ICFs. However, in all cases, these slopes are close to zero. In the worst case, $a = -0.08$, a metallicity variation equal to the complete metallicity range (1.5 dex, equivalent to a factor of about 32) implies a variation of the Ne/O ratio equal to 0.12 dex (equivalent to a factor of about 1.3). This Ne/O variation is very similar to the standard deviation of the data. We have also analysed the statistical depen-

dence of Ne/O with O/H using the Spearman rank correlation on the data. We have found that Ne/O is statistically constant, independent of the metallicity value. In another test, we considered the different metallicity regimes. We computed the average Ne/O value for the high [12+log(O/H) >8.2] and low [12+log(O/H) < 8.2] metallicity regime for each considered ICF. We list these results in Table 3. No variation of Ne/O with O/H is noted for these different regimes and for each ICF. Therefore, we can conclude that Ne/O and the metallicity have a flat relation for this sample. This flat Ne/O versus O/H behaviour for the whole range of O/H analysed is a robust test of nucleosynthesis prediction and supports a very

limited (if any) oxygen depletion in dust. The oxygen abundances in grains are poorly understood. For example, Izotov et al. (2006a) have suggested that the slight increase of Ne/O with the metallicity is the result of a depletion of about 20 per cent of O on to grains. Also, for three objects in a large range of metallicity, Peimbert & Peimbert (2010) have found an increasing depletion of O atoms, of about 0.1 dex, with increasing O/H. From our data, we have derived a dispersion of Ne/O for a fixed O/H value of ∼0.10 dex. Therefore, no conclusion can be obtained about the oxygen depletion on dust.

However, it must be noted that the scatter of Ne/O increases with the metallicity, giving the distribution of the data a triangular-like shape. This result was also found by Kennicutt et al. (2003) for H II regions in M101, NGC 2403 and dwarf irregular galaxies. They have argued that this effect can reflect high sensitivity to the local radiation field, because Ne^{++} and O^{++} become minor constituents of the nebular material when O^+/O increases, which is equivalent to a metallicity increment. As the metallicity of the gas material increases, the electron temperature decreases, and thus the Ne^{++} and O^{++} emission-line intensities become weak. Therefore, the increment of scatter going to higher abundances should be a normal behaviour, admitting that errors in the measurements of the sensitive lines are found to be larger (statistically) for higher abundance H II regions. In fact, the triangular shape mentioned is probably just

a product of this. We have also tested the dependence of Ne/O on the temperature fluctuations, because neon and oxygen have slightly different temperature coefficients. Using the earlier results of the models and computing Ne/H and O/H following the same procedure described in Section 4, we have found that log(Ne/O) is −0.53 and −0.36 for $P = 0.0$ and 0.01 pc, respectively. Thus, temperature fluctuations would not be a source of systematic errors in the Ne/O derivation.

Finally, we have tested the Ne/O dependence on the ionization degree $x = O^{++}/(O^+ + O^{++})$. To do this, we used the compiled sample to obtain the Ne/O abundances via the visible-lines method and the x values. The ICF for Ne from the IR-lines method (equation 15) was considered. In Fig. 14 (bottom panel), we can see that higher Ne/O values are found for objects with high excitation. This result is independent of the ICF considered. Although the neon ICF and O/H ratio decrease with x, the behaviour of the Ne/O ratio is a result of the increment in Ne^{++}/H^+ with x, as can be seen in Fig. 14 (top panel).

7 CONCLUSIONS

In this paper, we have shown that the ionic fractions Ne^{++}/H^+ obtained using the optical direct detections of the electron
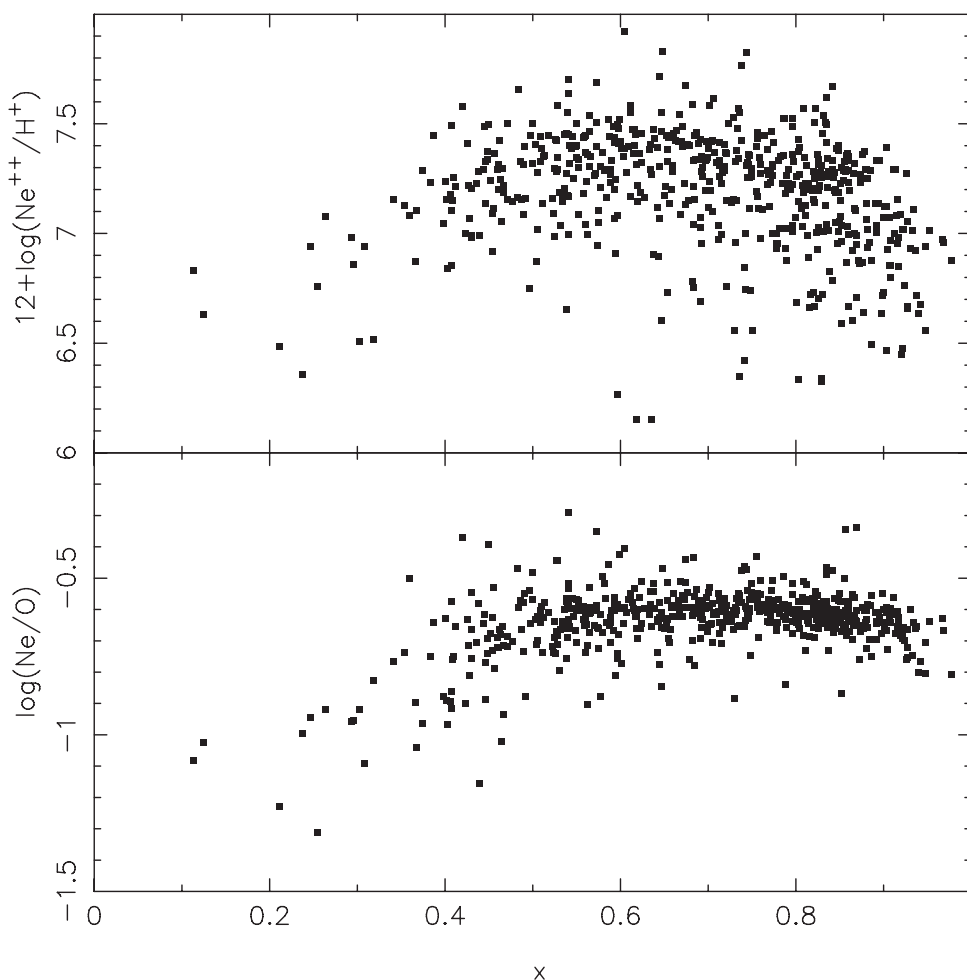
Figure 14. The bottom panel shows the relation between log(Ne/O) and the ionization degree $x = O^{++}/(O^+ + O^{++})$ obtained using the visible-lines method, the compiled sample and the ICF for Ne from the IR-lines method. Points represent estimations for the objects belonging to groups A and B. The top panel shows the relation between estimations of $12+\log(Ne^{++})/H^+$ and x.

temperature are underestimated by about a factor of 4 in relation to those estimated by mid-IR emission lines. We have discussed several possible causes of this discrepancy, including the following.

(i) Different apertures between optical and mid-IR observations, as already suggested by Vermeij & van der Hulst (2002). This effect should not be of great importance for most objects of the analysed sample, which behave as point-like sources. Besides, this effect has minimum effect in a high-excitation ion such as Ne^{++}.

(ii) Differential extinction effects. Mid-IR emission lines are possibly tracing a deeper ionization structure than optical ones. Besides, there are no reliable measurements of the $H\mu\alpha$ hydrogen recombination line at $10.52\ \mu m$, because it is blended with an H_2 line, so ionic abundances have been derived in relation to $H\beta$ or $Br\beta$ emission lines. We have not found any correlation between the degree of discrepancy and the inner extinction found from the Balmer decrement.

(iii) Uncertainties in the atomic data related with the IR emission of both [Ne II] and [Ne III]. These emission lines present some problems, as shown when inspecting the right lower panel of Fig. 1, where the observational data and photoionization models are shown. According to this figure, the models predict systematically lower values of the mid-IR [Ne III]/[Ne II] emission-line ratio than observations. This discrepancy has already been found by Morisset et al. (2004) and Pérez-Montero & Vílchez (2009), and apparently it is not related to the shape of the spectral energy distribution used in the models. The values for the [Ne III]$\lambda 15.56\mu m$ emission-line collision strength found in the literature over several decades differ by about 50 per cent. Even when we assume that the collision strength for [Ne III]$\lambda 15.56\ \mu m$ varies by a factor of 2, it is not enough to conciliate the neon ionic abundance discrepancy.

(iv) Variations of chemical abundances across the nebula. Using a grid of photoionization models, we have shown that fluctuations with an amplitude of 0.8 dex in the total abundance (for both O and Ne) can produce a degree of discrepancy between the ionic Ne^{++} abundances derived from optical and mid-IR emission lines.

Using ionic Ne abundance estimations from mid-IR emission lines, we have obtained an expression for the ICF of Ne^{++} as a function of the $O^{++}/(O^{+}+O^{++})$ ratio. These ICFs, obtained through the use of empirical and theoretical derivations of Ne^{++} from mid-IR lines, come from a quotient of emissivities and therefore minimize the impact of points (ii) and (iii) mentioned above, which are more critical for the abundance in absolute value. We have employed a large sample of observational spectroscopic data of star-forming regions, compiled from the literature, to analyse the dependence of the Ne/O abundance ratio on O/H. We have found that Ne/O is about constant with O/H ($\log Ne/O \approx -0.70$) for the whole metallicity range considered. This result is independent of the approximation adopted for the ICF, and in all cases the average Ne/O estimated for our sample is consistent with the adopted solar value.

ACKNOWLEDGEMENTS

REFERENCES

Allende Prieto C., Lambert D. L., Asplund M., 2001, ApJ, 556, L63
Amorín R., Vílchez J. M., Hägele G. F., Firpo V., Pérez-Montero E., Papaderos P., 2012, ApJ, 754, L22
Badnell N. R., et al., 2006, in Barlow M. J., Mendez R. H., eds, Proc. IAU Symp. 234, Planetary Nebulae in our Galaxy and Beyond. Cambridge Univ. Press, Cambridge, p. 211
Baldwin J. A., Phillips M. M., Terlevich R., 1981, PASP, 93, 5
Bergvall N., Östlin G., 2002, A&A, 390, 891
Blaha M., 1969, A&A, 1, 42
Bresolin F., 2011, ApJ, 730, 129
Bresolin F., Garnett D. R., Kennicutt R. C., 2004, ApJ, 615, 228
Bresolin F., Shaerer D., González Delgado R. M., Stasńska G., 2005, A&A, 441, 981
Bresolin F., Gieren W., Kudritzki R., Pietrzyński G., Urbaneja M. A., Carraro G., 2009, ApJ, 700, 309
Butler K., Zeippen C. J., 1994, A&AS, 108, 1
Calzetti D., Harris J., Gallagher J. S., Smith D. A., Conselice C. J., Homeier N., Kewley L., 2004, AJ, 127, 1405
Copetti M. V. F., 2006, A&A, 453, 943
Copetti M. V. F., Mallmann J. A. H., Schmidt A. A., Castañeda H. O., 2000, A&A, 357, 621
Crockett N. R., Garnett D. R., Massey P., Jacoby G., 2006, ApJ, 637, 741
Dinerstein H. L., Lester D. F., Werner M. W., 1985, ApJ, 291, 561
Dors O. L., Copetti M. V. F., 2003, A&A, 404, 969
Dors O. L., Copetti M. V. F., 2005, A&A, 437, 837
Dors O. L., Jr, Krabbe A., Hägele G. F., Pérez-Montero E., 2011, MNRAS, 415, 3616
Drake J. J., Testa P., 2005, Nat, 436, 525
Dufour R. J., Harlow W. V., 1977a, PASP, 89, 630
Dufour R. J., Harlow W. V., 1977b, ApJ, 216, 706
Engelbracht C. W., Rieke G. H., Gordon K. D., Smith J.-D. T., Werner M. W., Moustakas J., Willmer C. N. A., Vanzi L., 2008, ApJ, 678, 804
Ercolano B., Bastian N., Stasińska G., 2007, MNRAS, 379, 945
Esteban C., Bresolin F., Peimbert M., Garcia-Rojas J., Peimbert A., Mesa-Delgado A., 2009, ApJ, 700, 654
Ferland G. J., Korista K. T., Verner D. A., Ferguson J. W., Kingdon J. B., Verner E. M., 1998, PASP, 110, 761
Firpo V., Bosch G., Hägele G. F., Morrell N., 2010, MNRAS, 406, 1094
Firpo V., Bosch G., Hägele G. F., Díaz A. I., Morrell N., 2011, MNRAS, 414, 3288
Förster N. M. S., Genzel R., Lutz D., Kunze D., Sternberg A., 2001, ApJ, 552, 544
García-Rojas J., Esteban C., Peimbert M., Costado M. T., Rodríguez M., Peimbert A., Ruiz M. T., 2006, MNRAS, 368, 253
Garnett D. R., Shields G. A., Skillman E. D., Sagan S. P., Dufour R. J., 1997, ApJ, 489, 63
Garnett D. R., Edmunds M. G., Henry R. B. C., Pagel B. E. J., Skillman E. D., 2004, AJ, 128, 2772
Gordon K. L., Engelbracht C. W., Rieke G. H., Misselt K. A., Smith J.-D. T., Kennicutt R. C. Jr, 2008, ApJ, 682, 336
Grevesse N., Sauval A. J., 1998, Space Sci. Rev., 85, 161
Griffin D. C., Mitnik D. M., Badnell N. R., 2001, J. Phys. B: At. Mol. Opt. Phys., 34, 4401
Guseva N. G., Izotov Y. I., Thuan T. X., 2000, ApJ, 531, 776
Guseva N. G., Izotov Y. I., Papaderos P., Fricke K. J., 2007, A&A, 464, 885
Guseva N. G., Izotov Y. I., Stasińska G., Fricke K. J., Henkel C., Papaderos P., 2011, A&A, 529, 149
Hägele G. F., Pérez-Montero E., Díaz A. I., Terlevich E., Terlevich R., 2006, MNRAS, 372, 293
Hägele G. F., Díaz A. I., Terlevich E., Terlevich R., Pérez-Montero E., Cardaci M. V., 2008, MNRAS, 383, 209
Hägele G. F., Díaz A. I., Cardaci M. V., Terlevich E., Terlevich R., 2010, MNRAS, 402, 1005

Hägele G. F., García-Benito R., Pérez-Montero E., Díaz Á. I., Cardaci M. V., Firpo V., Terlevich E., Terlevich R., 2011, MNRAS, 414, 272
Hägele G. F., Firpo V., Bosch G., Díaz A. I., Morrell N., 2012, MNRAS, 422, 3475
Hägele G. F., Díaz A. I., Terlevich R., Terlevich E., Bosch G. L., Cardaci M. V., 2013, MNRAS, in press (doi:10.1093/mnras/stt491).
Heydari-Malayeri M., Le Bertre T., Magain P., 1988, A&A, 195, 230
Heydari-Malayeri M., Charmandaris V., Deharveng L., Meynadier F., Rosa M. R., Schaerer D., Zinnecker H., 2002, A&A, 381, 941
Izotov Y. I., Thuan T. X., 1998, ApJ, 500, 188
Izotov Y. I., Thuan T. X., 2004, ApJ, 602, 200
Izotov Y. I., Thuan T. X., Lipovetsky V. A., 1994, 435, 647
Izotov Y. I., Thuan T. X., Lipovetsky V. A., 1997, ApJS, 108, 1
Izotov Y. I., Chaffee F. H., Green R. F., 2001, ApJ, 562, 727
Izotov Y. I., Stasińska G., Meynet G., Guseva N. G., Thuan T. X., 2006a, A&A, 448, 955
Izotov Y. I., Schaerer D., Blecha A., Royer F., Guseva N. G., North P., 2006b, A&A, 459, 71
Kaufman V., Sugar J., 1986, J. Phys. Chem. Ref. Data, 15, 321
Kennicutt R. C., Bresolin F., Garnett D. R., 2003, ApJ, 591, 801
Kessler M. F. et al., 1996, A&A, 315, L27
Kewley L. J., Dopita M. A., Sutherland R. S., Heisler C. A., Trevena J., 2001, ApJ, 556, 121
Kewley L. J., Jansen R. A., Geller M. J., 2005, PASP, 117, 227
Kewley L. J., Groves B., Kauffmann G., Heckman T., 2006, MNRAS, 372, 961
Kingdon J. B., Ferland G. J., 1995, ApJ, 450, 691
Kingdon J. B., Ferland G. J., 1998, ApJ, 506, 323
Kobulnicky H. A., Skillman E. D., Roy J.-R., Walsh J. R., Rosa M. R., 1997, ApJ, 477, 679
Kobulnicky H. A., Kennicutt R. C., Pizagno J. L., 1999, ApJ, 514, 544
Krabbe A. C., Copetti M. V. F., 2002, A&A, 387, 295
Krabbe A. C., Copetti M. V. F., 2005, A&A, 443, 981
Krabbe A. C., Copetti M. V. F., 2006, A&A, 450, 159
Kwitter K. B., Aller L. H., 1981, MNRAS, 195, 939
Lebouteiller V., Bernard-Salas J., Brandl B., Whelan D. G., Wu Y., Charmandaris V., Devost D., Houck J. R., 2008, ApJ, 680, 398
Lee H., Skillman E. D., 2004, ApJ, 614, 698
Lee J. C., Salzer J. J., Melbourne J., 2004, ApJ, 616, 752
Leitherer C. et al., 1999, ApJS, 123, 3
Liu X-W., Storey P. J., Danziger I. J., Cohen M., Bryce M., 2000, MNRAS, 312, 585
López-Sánchez A. R., Esteban C., 2009, A&A, 508, 615
McCall M. L., Rybski P. M., Shields G. A., 1985, ApJS, 57, 1
McLaughlin B. M., Bell K. L., 2000, J. Phys. B: At. Mol. Opt. Phys., 33, 597
McLaughlin B. M., Lee T-G., Ludlow J. A., Landi E., Loch S. D., Pindzola M. S., Ballance C. P., 2011, J. Phys. B: At. Mol. Opt. Phys., 44, 5206
Masegosa J., Moles M., Campos-Aguilar A., 1994, ApJ, 420, 576
Mendoza C., 1983, in Flower D. R., ed., Proc. IAU Symp. 103, Planetary Nebulae. Reidel, Dordrecht, p. 143
Mesa-Delgado A., Núñez-Díaz M., Esteban C., García-Rojas J., Flores-Fajardo N., López-Martín L., Tsamis Y. G., Henney W. J., 2012, MNRAS, 426, 614
Morisset C., Schaerer D., Bouret J.-C., Martins F., 2004, A&A, 415, 577
Moustakas J., Kennicutt R. C., 2006a, ApJS, 164, 81
Moustakas J., Kennicutt R. C., 2006b, ApJ, 651, 155
Nagao T., Maiolino R., Marconi A., 2006, A&A, 459, 85

Nollenberg J., Skillman E., Garnett D. R., Dinerstein H., 2002, ApJ, 581, 1002
Oey M. S., Dopita M. A., Shields J. C., Smith R. C., 2000, ApJS, 128, 511
Oey M. S. et al., 2007, ApJ, 661, 801
Oliveira V. A., Copetti M. V. F., Krabbe A. C., 2008, A&A, 492, 463
Osterbrock D. E., 1989, Astrophysics of Gaseous Nebulae and Active Galactic Nuclei. University Science Books, Mill Valley, CA
Papaderos P., Guseva N. G., Izotov Y. I., Fricke K. J., 2008, A&A, 491, 113
Peimbert M., 1967, ApJ, 150, 825
Peimbert A., 2003, ApJ, 584, 735
Peimbert M., Costero R., 1969, Bol. Obs. Tonantzintla y Tacubaya, 5, 3
Peimbert A., Peimbert M., 2010, ApJ, 724, 791
Pérez-Montero E., Contini T., 2009, MNRAS, 398, 949
Pérez-Montero E., Díaz A. I., 2003, MNRAS, 346, 105
Pérez-Montero E., Vílchez J. M., 2009, MNRAS, 400, 1721
Pérez-Montero E., Hägele G. F., Contini T., Díaz A. I., 2007, MNRAS, 381, 125
Pilyugin L. S., 2001, A&A, 369, 594
Pilyugin L. S., Vílchez J. M., Contini T., 2004, A&A, 425, 849
Rubin R. H., 1985, ApJS, 57, 349
Rubin R. H., 1989, ApJS, 69, 897
Rubin R. H., Dufour R. J., Geballe T. R., Colgan S. W. J., Harrington J. P., Lord S. D., Liao A. L., Levine D. A., 2001, in Ferland G., Savin D. W., eds, ASP Conf. Ser. Vol. 247, Spectroscopic Challenges of Photoionized Plasmas. Astron. Soc. Pac., San Francisco, p. 479
Rubin R. H., Bhatt N. J., Dufour R. J., 2002, MNRAS, 334, 777
Rubin R. H. et al., 2007, MNRAS, 377, 1407
Rubin R. H. et al., 2008, MNRAS, 387, 45
Simpson J. P., 1975, A&A, 39, 43
Simpson J. P., Colgan S. W. J., Cotera A. S., Erickson E. F., Haas M. R., Morris M., Rubin R. H., 1997, ApJ, 487, 689
Skillman E. D., Terlevich R., Melnick J., 1989, MNRAS, 240, 563
Storey P. J., Hummer D. G., 1995, MNRAS, 272, 41
Tang S., Wang Q. D., Mac Low M., Joung M. R., 2009, MNRAS, 398, 1468
Thuan T. X., Izotov Y. I., 2005, ApJS, 161, 240
Torres-Peimbert S., Peimbert M., Fierro J., 1989, ApJ, 345, 186
van Hoof P. A. M., Weingartner J. C., Martin P. G., Volk K., Ferland G. J., 2001, in Ferland G., Savin D., eds, ASP Conf. Ser. Vol. 247, Spectroscopic Challenges of Photoionized Plasmas. Astron. Soc. Pac., San Francisco, p. 363
van Zee L., 2000, ApJ, 543, L31
van Zee L., Salzer J. J., Haynes M. P., O'Donoghue A. A., Balonek T. J., 1998, AJ, 116, 2805
Vermeij R., van der Hulst J. M., 2002, A&A, 391, 1081
Vermeij R., Damour F., van der Hulst J. M., Baluteau J.-P., 2002, A&A, 390, 649
Vílchez J. M., Iglesias-Páramo J., 2003, ApJS, 145, 225
Vílchez J. M., Pagel B. E. J., Díaz A. I., Terlevich E., Edmunds M. G., 1988, MNRAS, 235, 633
Wang W., Liu X-W., 2008, MNRAS, 389L, 33
Wesson R., Stock D. J., Scicluna P., 2012, MNRAS, 422, 3516
Willner S. P., Nelson-Patel K., 2002, ApJ, 568, 679
Woosley S. E., Weaver T. A., 1995, ApJS, 101, 181
Wu Y., Bernard-Salas J., Charmandaris V., Lebouteiller V., Hao L., Brandl B. R., Houck J. R., 2008, ApJ, 673, 193

This paper has been typeset from a TeX/LaTeX file prepared by the author.